Regime-dependent sensitivity of the atmospheric potential gradient to anthropogenic air pollution in São Paulo, Brazil

Rubén M. Romero[1], J.C. Tacza[2], Angel Vara-Vela[3], S. Szpigel[1], J.-P. Raulin[1]

[1] Center for Radio Astronomy and Astrophysics Mackenzie, Engineering School, Mackenzie Presbyterian University, São Paulo, Brazil.
[2] Institute of Geophysics, Polish Academy of Sciences, Warsaw, Poland.
[3] Institute of Physics, University of São Paulo, Rua do Matão, 1371, Cidade Universitária, 05508-090, São Paulo, Brazil

Abstract:

Ground-based measurements of the atmospheric potential gradient (PG) are sensitive to near-surface electrical conductivity and can reflect anthropogenic perturbations under carefully defined fair-weather (FW) conditions. This study investigates the coupling between PG and major air pollutants in São Paulo, Brazil, using a long-term dataset (2018–2024) combining rooftop electric field measurements with hourly concentrations of CO, SO_2, NO, NO_2, NO_x, and PM_{10}. FW periods were identified using surface meteorological screening and satellite-based cloud masking.

The analysis reveals a reproducible hierarchy in PG–pollutant coupling controlled by the dynamical regime of the atmospheric boundary layer. During nocturnal stable conditions, primary combustion-related gases (NO_x, NO, CO) exhibit the strongest associations with PG, with median Pearson correlation coefficients (r) on the order of $r \approx 0.6$, representing the central tendency of a regime-dependent distribution. In contrast, PM_{10} shows weaker and more variable coupling. Across all seasons, PG–pollutant correlations strengthen at night and weaken markedly during the afternoon mixing maximum, with enhanced wind ventilation further suppressing coupling strength.

Large-scale emission perturbations support the anthropogenic origin of these relationships. During the 2020 COVID-19 lockdown, FW PG exhibits a persistent shift toward lower values relative to the multi-year baseline while preserving the diurnal phase structure. In contrast, a short (11-day) truck drivers' strike in 2018 produces no statistically distinguishable PG response.

These results demonstrate that PG is not a universal proxy for urban air pollutant concentrations, but a regime-dependent electrical indicator whose sensitivity to anthropogenic emissions emerges preferentially under stable boundary-layer conditions in a megacity environment.

Keywords:

Atmospheric electricity, Potential gradient, Air pollution, Boundary layer, Urban environment, Megacity

Highlights:

- Fair weather conditions are partially defined using satellite cloud screening.
- PG shows a pollutant sensitivity hierarchy, stronger for NOx and CO than PM10.
- PG–pollutant correlations weaken during afternoon convective mixing, even cloud-free.
- Fair-weather PG shows a persistent reduction during the 2020 COVID-19 lockdown.
- Linear models capture nocturnal coupling; nonlinear models perform better diurnally.

Graphical abstract:

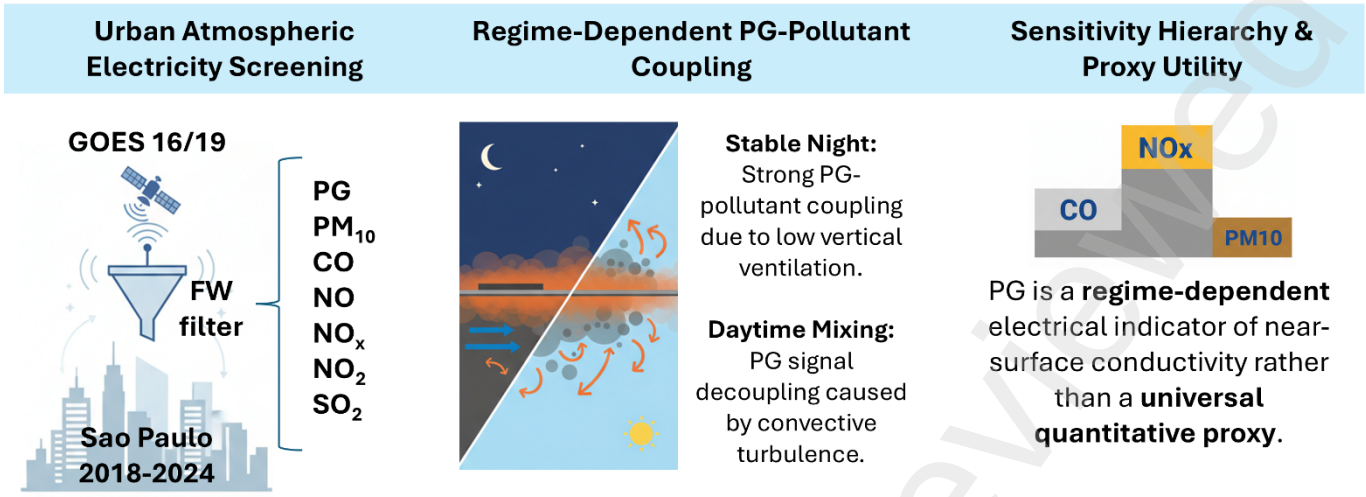

1. Introduction

The Earth's atmosphere sustains a persistent vertical electric field, globally maintained by the Global Atmospheric Electric Circuit (GAEC). This system can be conceptualized as a planetary-scale capacitor, with the conductive Earth surface and the ionosphere acting as electrodes, separated by a weakly conducting atmosphere. Thunderstorms and electrified clouds serve as current sources, injecting positive charge upward, while under fair weather conditions, this charge returns gradually to the surface as a downward current that completes the global circuit (Wilson, 1921; Whipple, 1929; Rycroft et al., 2000).

A key observable manifestation of the GAEC at the ground is the atmospheric potential gradient (PG), which represents the vertical atmospheric electric field. Following the conventional sign convention of atmospheric electricity, the potential gradient is defined as PG = -Ez where Ez is the vertical component of the field, taken as positive upward. Under this convention, a positive PG corresponds to an increase of electric potential with height (Chalmers, 1954). Hereafter, ground-based measurements of the atmospheric electric field are referred to in terms of the PG. In the late 1920s, ocean-based measurements were conducted by the Carnegie Institute. These campaigns revealed a remarkably consistent diurnal variation in the PG across different oceanic regions, a pattern now known as the Carnegie curve (Harrison, 2013). Under fair-weather conditions over the oceans, PG exhibits stable positive values of the order of 10^2 V/m, as established by the Carnegie expedition measurements (Mauchly, 1923). Because these measurements were taken far from local pollution sources, the Carnegie curve remains the global reference for undisturbed fair weather PG behavior. However, ground-level PG measurements are highly sensitive to local disturbances, including meteorological variability and pollution-related aerosol loading.

A key factor mediating this sensitivity is the structure of the atmospheric boundary layer, commonly characterized by its height (BLH), which defines the effective dilution volume for aerosols and trace gases and controls the degree of coupling between surface measurements and the overlying atmosphere (Kotthaus et al., 2023).

At continental and urban sites, numerous studies have confirmed that PG responds not only to meteorological disturbances such as precipitation, wind, and cloud cover (Bennett and Harrison, 2007; Karagioras and Kourtidis, 2021), but also to anthropogenic emissions. In the UK, Wright et al. (2019) found a positive relationship between PG and aerosol loading expressed in terms of particle number concentration rather than mass-based PM metrics during pollution events. More recently, Yaniv et al. (2026) demonstrated in the Tel Aviv metropolitan area that PG exhibits strong, near-synchronous diurnal

and weekly coupling with traffic-related NOx, while its relationship with PM2.5 is weaker and temporally lagged, reflecting differences in aerosol residence time and microphysical interactions.

In India, Faruque et al. (2025) reported PG–AQI (Air Quality Index) correlations with seasonal variability and polarity reversals. In Buenos Aires, Argentina, Velázquez et al. (2025) linked PG with NO_2 levels and vehicular traffic, observing clear weekly cycles as well as a significant PG reduction (~15%) during the COVID-19 lockdown, attributed to decreased vehicular activity. These recent findings, including those from pandemic-related emission drops, reinforce early observations by Sheftel et al. (1994), who reported systematic weekly variations in PG and air conductivity between weekdays and Sundays in industrial regions, highlighting the sensitivity of PG to human activity patterns. The unprecedented reduction in human activity during the COVID-19 lockdown therefore provides a unique natural experiment to explore anthropogenic influences on PG variability.

The underlying physical mechanism explaining this PG sensitivity is well-established. Small ions generated by cosmic rays and natural radioactivity are the main contributors to atmospheric conductivity due to their high mobility (Cobb, 1973). When aerosol concentrations are elevated, these ions attach to particles, forming larger, slower-moving charged clusters (Dhanorkar and Kamra, 1992; Harrison and Carslaw, 2003). This process reduces the air's conductivity, and as a result, following Ohm's law ($E = J/\sigma$), the atmospheric electric field increases (Chalmers, 1954; Piper and Bennett, 2012). Under extreme pollution conditions, a negative space charge layer can develop near the surface, even leading to polarity inversion (Faruque et al., 2025).

While the ion–aerosol mechanism linking pollution and PG is well established, its manifestation in ground-based observations is strongly modulated by local and regional processes. Previous studies have shown that ground-based PG measurements are highly sensitive to aerosol-related processes even under nominal fair-weather conditions. In particular, Romero et al. (2024) demonstrated that natural aerosol loading and wind-driven particle transport can induce substantial PG anomalies in the absence of strong anthropogenic emissions. Similar conclusions were reached by Nicoll et al. (2022) at an arid desert site, where local dust lofting, sea-breeze circulations, and convection were shown to dominate PG variability even under meteorologically fair conditions, thereby illustrating that fair weather does not necessarily imply electrically undisturbed conditions. These findings highlight the need for careful filtering and cautious interpretation of PG variability.

In urban environments such as São Paulo, a wide range of air pollutants can influence atmospheric conductivity through ion–aerosol interactions. Carbon monoxide (CO), mainly produced by incomplete combustion processes, especially from motor vehicles and biomass burning, represents a significant fraction of urban pollution, while nitrogen oxides (NO and NO_2), sulfur dioxide (SO_2), and particulate matter (PM_{10}) reflect the combined influence of local emissions and regional aerosol transport, particularly during the dry season and biomass burning periods (Vara-Vela et al., 2018; Mohammed et al., 2020; Coelho et al., 2023). These substances play a central role in capturing atmospheric ions and modifying the PG under fair-weather conditions (Harrison and Carslaw, 2003), enabling the use of PG as a proxy for urban aerosol loading in historical and modern datasets (Harrison and Aplin, 2003).

In South America, Tacza et al. (2020) showed that PG measurements at urban sites such as São Paulo (SPA), located in the city center and exposed to intense vehicular traffic, deviate significantly from the Carnegie curve, displaying a low correlation ($r \approx 0.66$). In contrast, the El Leoncito station (CAS), situated at 2480 m altitude in the remote Argentine Andes, far from urban activity and characterized by persistently clear skies, retains a strong correlation with the global signal ($r \geq 0.9$). This contrast highlights how urban pollution can distort the PG signal, while remote high-altitude stations provide a more accurate representation of the global atmospheric electric circuit.

The 2019 "black rain" event in São Paulo, caused by smoke from intense Amazonian fires, further illustrates the city's exposure to complex and long-range aerosol pollution. As documented by Pereira et al. (2021) and Vara-Vela et al. (2021), this episode brought unusually dark and turbid rain, linked to the deposition of biomass burning residues transported over hundreds of kilometers. Such events underscore the need to disentangle local from regional pollution effects when interpreting PG variability in megacities.

Despite the established physical link between aerosols and atmospheric conductivity, the application of data-driven models to exploit this relationship remains limited. Recent studies have successfully applied Machine Learning (ML) techniques to PG data; for instance, Guo et al. (2017) and Bao et al. (2022) utilized neural networks to forecast PG intensity for lightning warning systems. Regionally, Soria et al. (2020) applied similar models to predict PG variability in Lima, Peru. However, these works focus on predicting the electrical parameter itself. To date, the inverse approach, leveraging the high-response PG sensor as a physical input feature to estimate urban pollution levels (e.g., PM_{10}), remains largely unexplored in the literature, representing a novel application of atmospheric electricity data in environmental monitoring.

The main objective of this study is to evaluate whether PG can serve as a reliable proxy for anthropogenic air pollution in São Paulo by correlating PG with PM_{10}, NO_x, SO_2, and CO concentrations from 2018 to 2024 under fair-weather conditions. In addition to correlation analyses, this study proposes a machine learning framework based on Random Forest to test the predictive capability of PG for urban air pollution. Weekly and seasonal PG patterns are also analyzed to assess the signature of urban activity on the PG, thereby exploring the potential of rigorously filtered PG measurements as a physically meaningful indicator of urban aerosol loading in São Paulo.

2. Study Area and Data Sources

2.1. Study Area

The study was conducted in São Paulo, one of the largest and most polluted megacities in the Southern Hemisphere, characterized by a subtropical climate with dry winters and wet summers (Andrade et al., 2017). The PG sensor used in this study is installed on the rooftop of Building 45 – Center for Social and Applied Sciences (CCSA) at Mackenzie Presbyterian University, located in the central district of Consolação (latitude: 23.547515°S, longitude: 46.652334°W). Positioned approximately 37 meters above ground level, the sensor is operated by the Center for Radio Astronomy and Astrophysics Mackenzie (CRAAM) and it is part of the Atmospheric electric Field Network in South America (AFINSA), a coordinated initiative aimed at monitoring PG variations across the continent. In this study, the São Paulo station is hereafter referred to as SPA **(Figure 1).**

2.2 PG Dataset

The PG dataset covers the period from February 2018 to December 2024. Measurements were recorded using a Boltek EFM-100 electrostatic field mill installed at SPA. Data were acquired at high frequency (20 Hz) and stored in raw format. For consistency with other datasets, subsequent analyses were performed at hourly resolution.

As a complementary case, this study revisits a separate PG-only dataset from Ica (Peru), previously reported by Romero et al. (2024). These data are used exclusively for qualitative comparison during the early phase of the COVID-19 lockdown and do not form part of the main São Paulo analysis or the statistical framework of this study.

2.3 Air Quality Data

Complementary air quality measurements were obtained from the Cerqueira César (CQC) monitoring station. The instrument is located on the rooftop of the School of Public Health at the University of São

Paulo, in central São Paulo. This station is located approximately 2 km from the SPA sensor and is operated by the São Paulo Environmental Agency (CETESB, Companhia Ambiental do Estado de São Paulo). The station is situated in a densely urbanized environment characterized by intense vehicular traffic and heterogenous institutional land use.

According to the official site characterization and micro-inventory of emission sources provided by the São Paulo Environmental Agency, the surroundings of CQC location are dominated by mobile emission sources, primarily traffic along major avenues. No significant industrial point sources are identified within a radius of approximately 2 km. Fixed emission sources in the immediate vicinity are limited to small commercial activities (e.g., fuel stations and restaurant ovens), while substantial portions of the surrounding area are occupied by green spaces, hospitals, and cemeteries (CETESB, 2005).

Hourly concentrations of CO, SO_2, NO, NO_2, NO_x, and PM_{10} were used in this study. All datasets were quality-controlled and validated by CETESB in accordance with national air-quality monitoring standards.

2.4 Meteorological Data

Meteorological observations were obtained from the three ground stations operated by the National Institute for Meteorology (INMET) that are closest to the PG and CQC sensors, namely Barueri, Mirante, and Interlagos. These stations form a triangular network with side lengths of ~26–30 km around São Paulo city, providing regional coverage of precipitation, temperature, humidity, irradiance, and wind. This configuration allows for independent assessment of local versus regional meteorological disturbances.

The SPA and CQC sensors are positioned near the northeastern vertex of this triangular region, as shown in **Figure 2**, which summarizes the spatial distribution of all monitoring sites.

2.5 Satellite Data

Geostationary satellite data were obtained from the Geostationary Operational Environmental Satellites GOES-16 and GOES-19, operated by the National Oceanic and Atmospheric Administration (NOAA) in collaboration with the National Aeronautics and Space Administration (NASA). The data were received, processed, and archived by the Brazilian National Institute for Space Research (Instituto Nacional de Pesquisas Espaciais, INPE) through its Center for Weather Forecasting and Climate Studies (Centro de Previsão de Tempo e Estudos Climáticos, CPTEC).

Full-disk Red–Green–Blue (RGB) composite imagery was accessed via the public CPTEC/INPE FTP repository (https://ftp.cptec.inpe.br), specifically from the GOES-R series directories corresponding to the 2018–2024 period. The RGB products are derived from measurements of the Advanced Baseline Imager (ABI) sensor and follow the standard processing chain implemented at the INPE GOES-R reception station (Uba et al., 2023).

The native temporal resolution of the full-disk imagery is 10 minutes. For consistency with the ground-based datasets, the satellite archive was subsampled at hourly intervals (top of the hour), yielding approximately 50,000 images over the study period. These data were used exclusively to support the classification of fair-weather conditions.

Figure 1. Three-dimensional view of the rooftop of Building 45 (CCSA) at Mackenzie Presbyterian University, São Paulo. The yellow location marker indicates the position of the PG sensor. Image obtained from Google Earth Pro, imagery date: February 26, 2025. © 2025 Airbus, Image: Landsat / Copernicus.

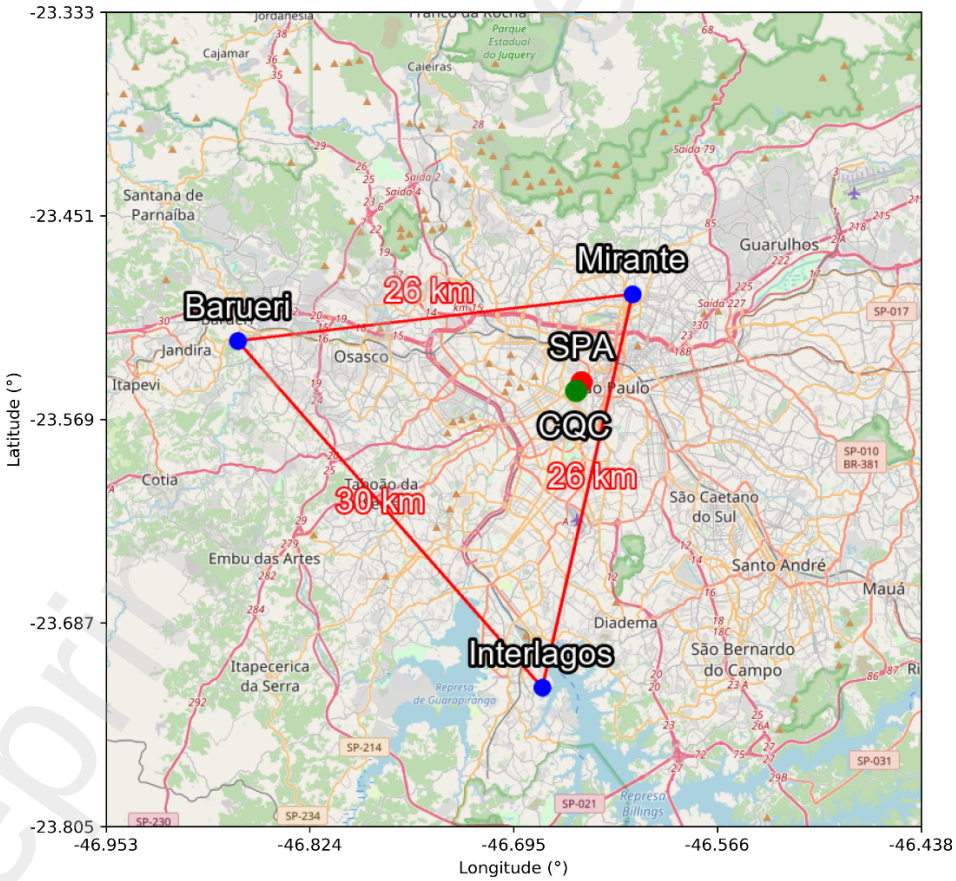

Figure 2. Spatial distribution of the monitoring sites in São Paulo. The PG sensor at SPA (red dot) is located in the city center. The CQC air quality station (green dot), approximately 2 km away, provides representative aerosol data. Meteorological stations at Barueri, Mirante, and Interlagos (blue dots) form a triangular network (~26–30 km sides) used to filter out precipitation and thunderstorm events, delimiting the fair weather observation region.

3. Methodology

3.1 Data Preprocessing

All datasets described in Section 2 were standardized to a common hourly temporal resolution to ensure internal consistency across analyses. Raw PG measurements were aggregated into hourly means, while the air quality, meteorological, and satellite datasets were already available at this temporal scale. Quality control procedures included the removal of instrumental artifacts, physically unrealistic values, and time intervals affected by sensor maintenance or data acquisition issues. Only validated observations were retained for subsequent analyses.

3.2 Fair-Weather Classification

Fair-weather (FW) conditions were defined using a two-step filtering procedure that combines ground-based meteorological observations with satellite-based cloud screening.

In the first step, hours with recorded precipitation were excluded based on surface meteorological records, since rainfall directly perturbs near-surface PG measurements and violates fair-weather conditions.

In the second step, a satellite-based cloud filter was applied using hourly imagery from the GOES-16 and GOES-19 platforms **(Figure 3)**. For each hour, the imagery was cropped to a 10 × 10 km domain centered on the SPA sensor. The local cloud fraction (CF) was computed as the ratio of cloud-covered pixels (N-cloud) to the total number of pixels (N-total) within the domain. All hours with a cloud fraction exceeding 20% were excluded.

$$\mathrm{CF}(\%) = 100 \times \frac{N_{\mathrm{cloud}}}{N_{\mathrm{total}}}$$

The choice of a limited spatial domain is motivated by the need to isolate cloud structures directly influencing the local PG. Larger domains may include mesoscale cloud systems located away from the sensor that do not affect local fair-weather conditions but can artificially inflate cloud-fraction estimates. Restricting the analysis to a 10 × 10 km window minimizes this bias and reduces false cloud detections associated with remote cloud structures. This two-step procedure yielded the general fair-weather hourly dataset, which constitutes the reference FW pool for all subsequent analyses.

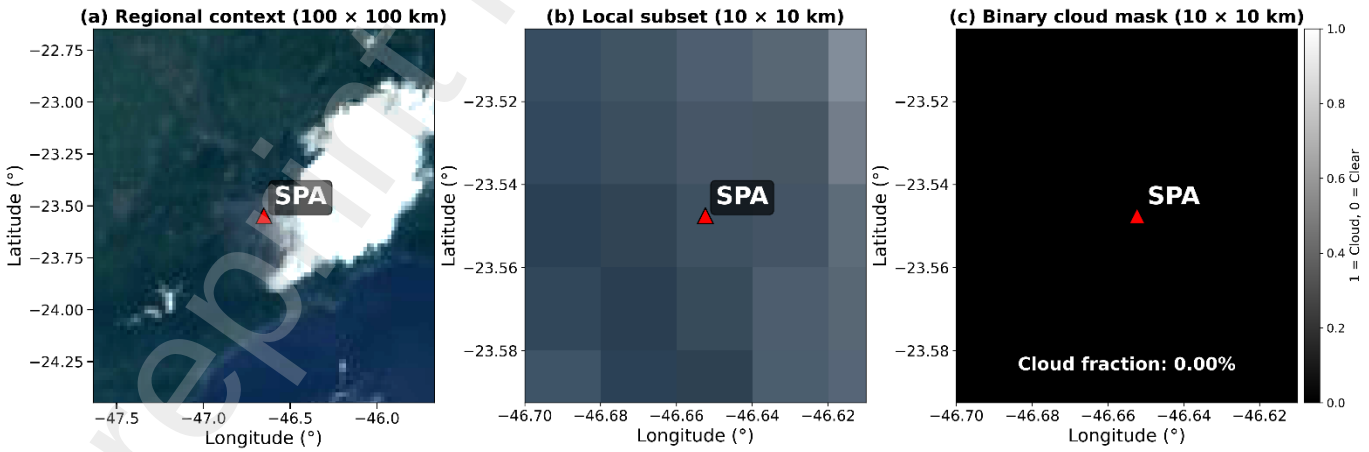

Figure 3. Example of the satellite-based cloud screening procedure applied for fair-weather classification. Panel (a) shows the regional context (100 × 100 km) derived from hourly GOES imagery around the measurement site. Panels (b) and (c) show the local domain (10 × 10 km): (b) enhanced visible imagery and (c) the corresponding binary cloud mask. The example corresponds to 9 February 2023 at 11:00 UTC and is shown for illustrative purposes.

Boundary-layer height is not directly observed in this study. Accordingly, references to nocturnal versus daytime “regimes” are used in an operational sense to distinguish dynamically stable, weakly ventilated conditions from convectively mixed states, rather than to imply explicitly retrieved BLH values. The analysis therefore focuses on separating electrically clean fair-weather periods and contrasting night-time accumulation versus daytime mixing based on the observed diurnal structure and surface meteorological context.

3.3 Construction of Analysis-Specific Subsets

From the general fair-weather hourly dataset, multiple analysis-specific subsets were constructed to address distinct scientific objectives. This separation ensures that each analysis is based on data with an appropriate level of temporal completeness and statistical robustness, while avoiding unnecessary data loss or over-filtering. Figure 4 summarizes the complete fair-weather data filtering workflow and illustrates how the different analysis-specific datasets are derived from the same general fair-weather hourly pool.

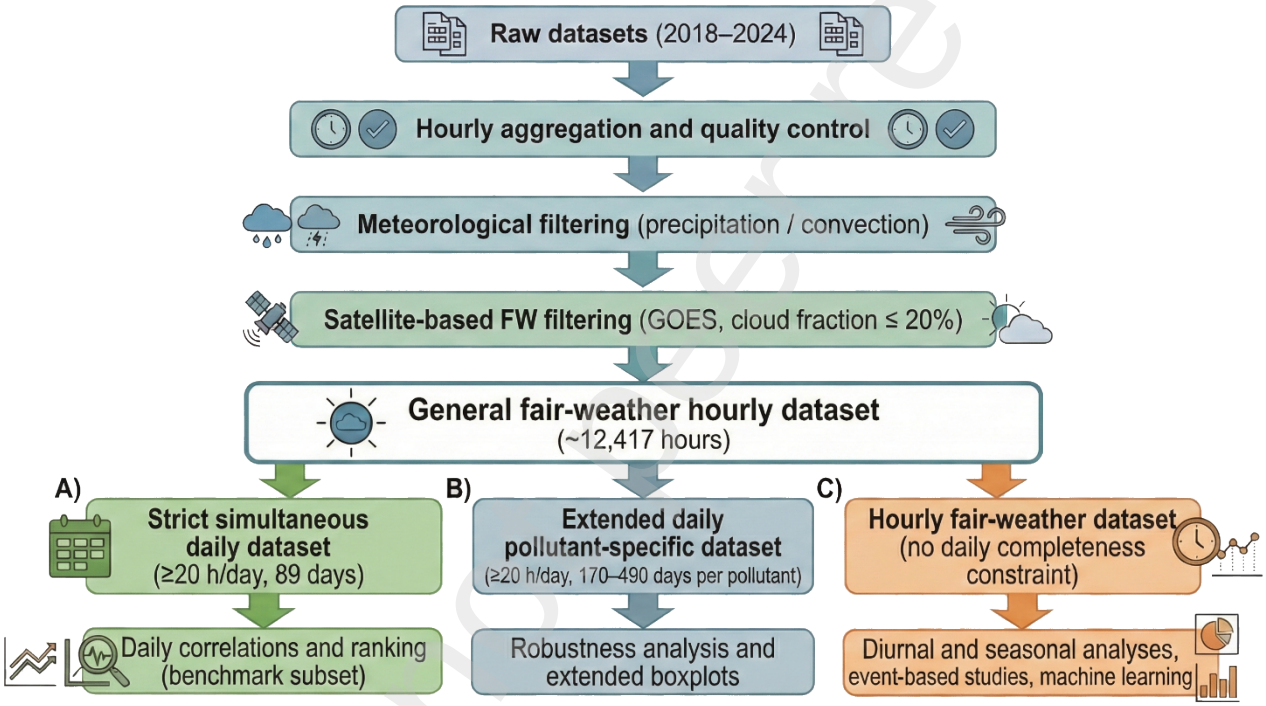

Figure 4. Workflow illustrating the construction and use of the fair-weather datasets.

3.3.1 Strict Daily Dataset

For analyses requiring strict inter-pollutant comparability at the daily scale, a stringent completeness criterion based on full simultaneity was applied. Only hours with simultaneous and valid records from the PG sensor and all six pollutant monitors were considered. From this pool, only days with at least 80% data coverage, corresponding to a minimum of 20 valid hourly records per day, were retained.

This strict daily dataset (n = 89 days) was used as a reference subset for the computation of daily PG–pollutant correlation coefficients, the construction of comparative correlation rankings and boxplots, and the evaluation of inter-pollutant consistency under fully simultaneous sampling conditions. By enforcing this strict completeness requirement, the resulting daily correlations are not affected by uneven temporal sampling or differential data availability across pollutants.

To assess the robustness of the inferred hierarchy, extended daily datasets were constructed by relaxing the simultaneity requirement while retaining the same hourly fair-weather filtering and daily completeness threshold. These extended daily datasets substantially increase data availability (approximately 170 to 490

valid days per pollutant) and are used for analyses requiring enhanced temporal coverage, such as event-based interpretation and meteorological case studies. Importantly, this extension does not alter the underlying fair-weather definition, but only the simultaneity constraint applied at the daily aggregation stage.

3.3.2 Hourly Fair-Weather Dataset

In parallel, the full general hourly fair-weather dataset, comprising approximately 12,417 hours (corresponding to roughly 517 equivalent days when expressed purely in hourly terms), was retained without imposing a daily completeness constraint. This dataset preserves the full temporal variability of atmospheric conditions under fair-weather regimes and provides a substantially larger sample size.

The hourly fair-weather dataset was used for analyses that do not require complete daily coverage, including scatterplot-based examinations of PG–pollutant relationships, assessments of diurnal and seasonal variability, and the development and evaluation of machine learning models. Retaining this broader dataset enables a more detailed exploration of continuous atmospheric processes while remaining fully consistent with the fair-weather definition.

Together, these two complementary subsets allow robust daily-scale statistics to be derived without sacrificing the statistical power and physical insight afforded by the full set of hourly observations.

3.4 Statistical Analysis

The relationship between the PG and air pollutant concentrations was quantified using both Pearson's correlation coefficient, which characterizes linear associations, and Spearman's rank correlation coefficient, which is less sensitive to outliers and captures monotonic but non-linear relationships. The combined use of these two metrics provides a comprehensive and robust characterization of PG–pollutant coupling across a wide range of atmospheric conditions.

3.5 Event-Based Analysis

Periods characterized by abrupt and externally driven changes in anthropogenic emissions were analyzed separately to assess the sensitivity of the PG to large-scale perturbations in air quality. Two such events were considered: the truckers' strike in May 2018 and the COVID-19 lockdown in 2020, both of which resulted in marked reductions in traffic and industrial activity in São Paulo (Leirião et al., 2020; Rudke et al., 2023).

For each event, PG behavior during the perturbation was compared against baseline periods before and after the event, allowing the magnitude and persistence of PG anomalies associated with reduced emissions to be quantified.

3.6 Machine Learning Approach

Using the general fair-weather hourly dataset described in Section 3.3.2, a machine learning (ML) framework was applied to explore the predictive relationship between atmospheric parameters and urban air pollution. The predictive task consisted of estimating surface concentrations of PM_{10}, CO, and NO_2 using a common set of predictors. Predictor variables (features) included hourly PG and meteorological factors such as mean relative humidity, mean wind speed, and mean wind direction (encoded as sine and cosine components). To account for temporal cycles, the hour of the day and the day of the year were also included as cyclical features (sine/cosine transformed) (Khaled et al., 2022).

Two complementary regression strategies were tested: Multiple Linear Regression (MLR) and a Random Forest (RF) regressor. MLR provides a simple and transparent baseline by modeling the pollutant

concentration as a linear combination of the input features, assuming additive and stationary relationships. This approach allows direct assessment of whether the PG–pollutant coupling can be adequately represented by a linear response under dynamically stable conditions.

In contrast, the RF model is an ensemble-based, non-parametric method that constructs a large number of decision trees using bootstrap sampling and random feature selection, and aggregates their predictions to reduce variance and improve generalization. RF can capture non-linear responses, interaction effects between predictors, and regime-dependent behavior without imposing an explicit functional form.

Physically, the interaction between aerosol concentration, near-surface ion balance, and atmospheric conductivity is expected to exhibit non-linear behavior due to ion attachment processes and saturation effects, as established in theoretical frameworks (Harrison & Carslaw, 2003).

Recent comprehensive reviews have shown that ensemble-based methods often outperform linear models and can achieve accuracy comparable to deep learning approaches when interpretability and robustness are required, particularly in station-based air-pollution applications (Karmoude et al., 2025; Peng et al., 2024). Within the broader context of data-driven air-pollution modeling, Bernacki and Scherer (2025) identify Random Forest as a reliable baseline for complex environmental datasets, supporting its use here as a reference non-linear model for atmospheric electrical proxies.

To evaluate the regime dependence of PG-based predictability, the ML analysis was performed under two predefined temporal windows representing contrasting boundary-layer dynamical conditions: a stable nocturnal period (UTC 00–12) and the full diurnal cycle (UTC 00–23). The dataset was split chronologically using a cut-off date of 1 January 2023. All data prior to this date were used for training, while all data from this date forward were used for testing, ensuring that model performance was evaluated under unseen and more recent conditions. Standard regression metrics were adopted for evaluation, including the coefficient of determination (R^2) and the mean absolute error (MAE). The RF hyperparameters were set empirically for the comparison.

Based on established boundary-layer theory and previous atmospheric electricity studies, model performance is expected to degrade during periods of enhanced turbulent mixing, when the physical coupling between the PG and pollutant concentrations weakens. More generally, recent reviews emphasize that the performance of machine-learning models for air-pollution prediction is strongly regime-dependent, varying with season, location, and concentration levels (Peng et al., 2024).

4. Results

4.1 Data quality and wind-field influence

The multi-stage filtering process described in the methodology defines the data basis for all subsequent analyses. Here, we quantify its impact on data availability over the study period, which spans from February 2018 to December 2024. After enforcing data simultaneity across all seven instruments, a total of 18,843 valid hourly records (~785 days in purely hourly terms) were retained. Application of the fair-weather classification reduced this pool by 34%, yielding a general fair-weather dataset of approximately 12,417 hours (~517 equivalent days). This flexible fair-weather hourly dataset constitutes the primary data basis for most analyses presented in this study, including hourly correlations, diurnal and seasonal variability, case studies, and machine learning applications. From this dataset, the daily completeness criterion resulted in a stricter subset of 89 days used specifically for daily-scale correlation analyses. **Figure 5** visually summarizes the impact of the fair-weather filtering on data availability, showing the daily fraction of retained (blue) and filtered-out (red) data over the study period.

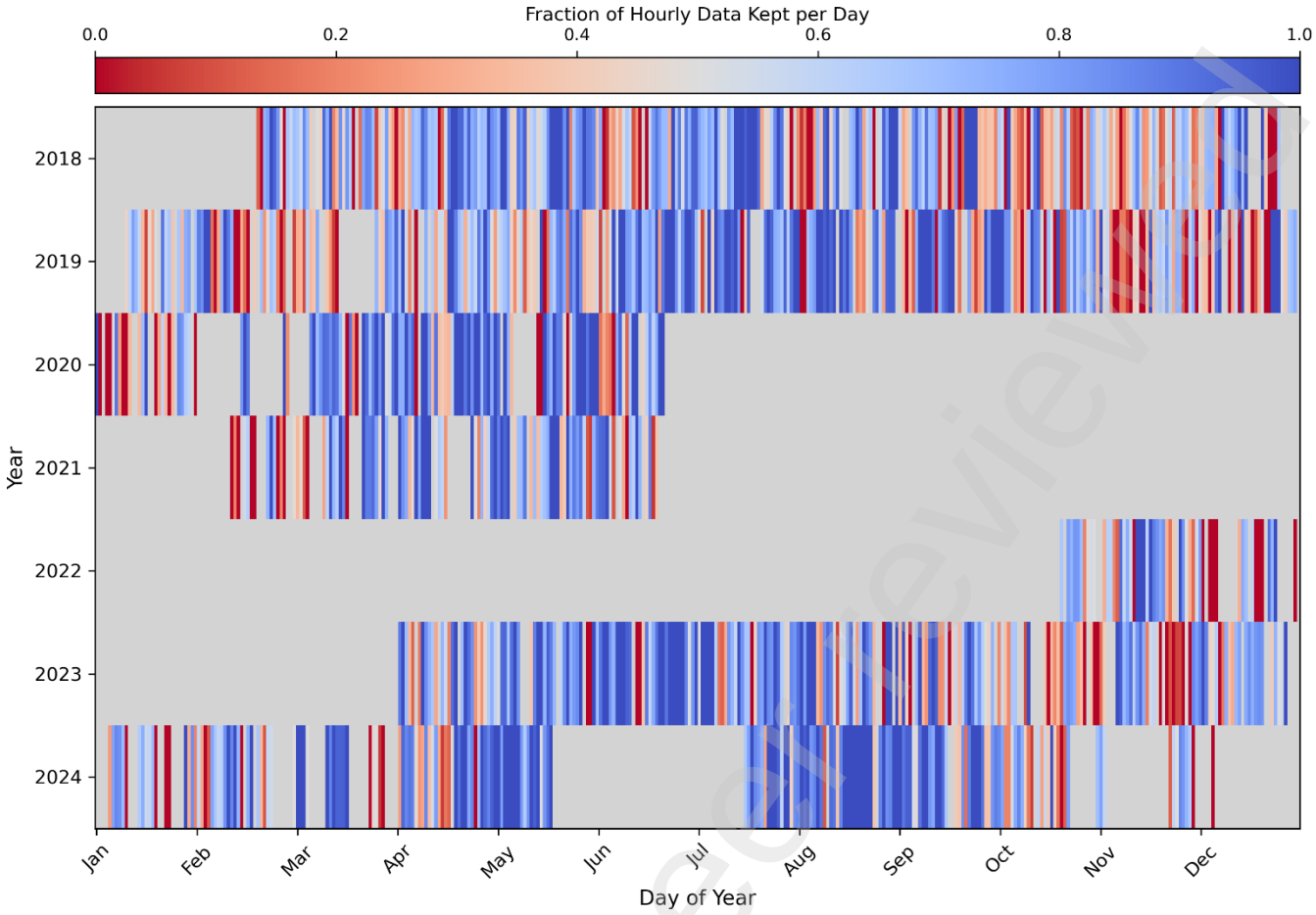

Figure 5. Matrix illustrating the daily availability of simultaneous PG and pollutant data from 2018 to 2024. The color of each day represents the fraction of hourly records retained after applying the fair-weather filter, which excludes hours with cloud cover exceeding 20%. Days in blue indicate that a high fraction of hours were retained, while days in red indicate a high fraction were removed due to clouds. Grey **color** indicates days with no initial simultaneous data.

We also examined whether wind speed acts as a dominant control on PG variability within the fair-weather dataset. Although some operational definitions adopt an upper wind-speed threshold (e.g., ~8 m s^{-1}), our entire dataset falls well below this limit, with maximum observed winds not exceeding 6.5 m s^{-1} (Fig. 6a–c). Our diagnostic analysis therefore focused on determining whether, even within this accepted fair-weather range, wind speed exerts a dominant influence on near-surface PG variability.

Figure 6 illustrates the pronounced diurnal cycle of wind speed and its systematic relationship with the PG. The top panels (Fig. 6a–c) reveal a clear daily pattern common to all three sites, characterized by minimum wind speeds (blue boxes) occurring during the stable nocturnal and early morning period between 04:00 and 10:00 UTC (01:00–07:00 LT). In sharp contrast, a consistent wind speed maximum (red boxes) is observed at 19:00 UTC (16:00 LT).

The bottom panels **(Fig. 6d-f)** quantify the impact of this meteorological cycle on the electrical environment. A persistent negative correlation is observed between wind speed and PG at all locations, with Pearson coefficients (R) ranging from -0.21 to -0.30. This relationship, quantified by slopes (m) between -0.11 and -0.15 kV/m per m/s, confirms the physical mechanism: stronger winds disperse the near-surface space charge layer, very likely through enhanced turbulent mixing, leading to lower PG values. Conversely, the calm wind conditions during the morning stability period **(Fig. 6a-c)** inhibit dispersion, allowing for the accumulation of aerosols and space charge. However, the relatively weak correlation magnitudes indicate that wind speed does not dominate PG variability within this low-wind fair-weather regime. This result

empirically justifies the decision not to impose an additional wind-speed filter in the fair-weather classification. This behavior persists across seasons, with a stronger coupling during winter (Appendix A, Figs. A1–A4).

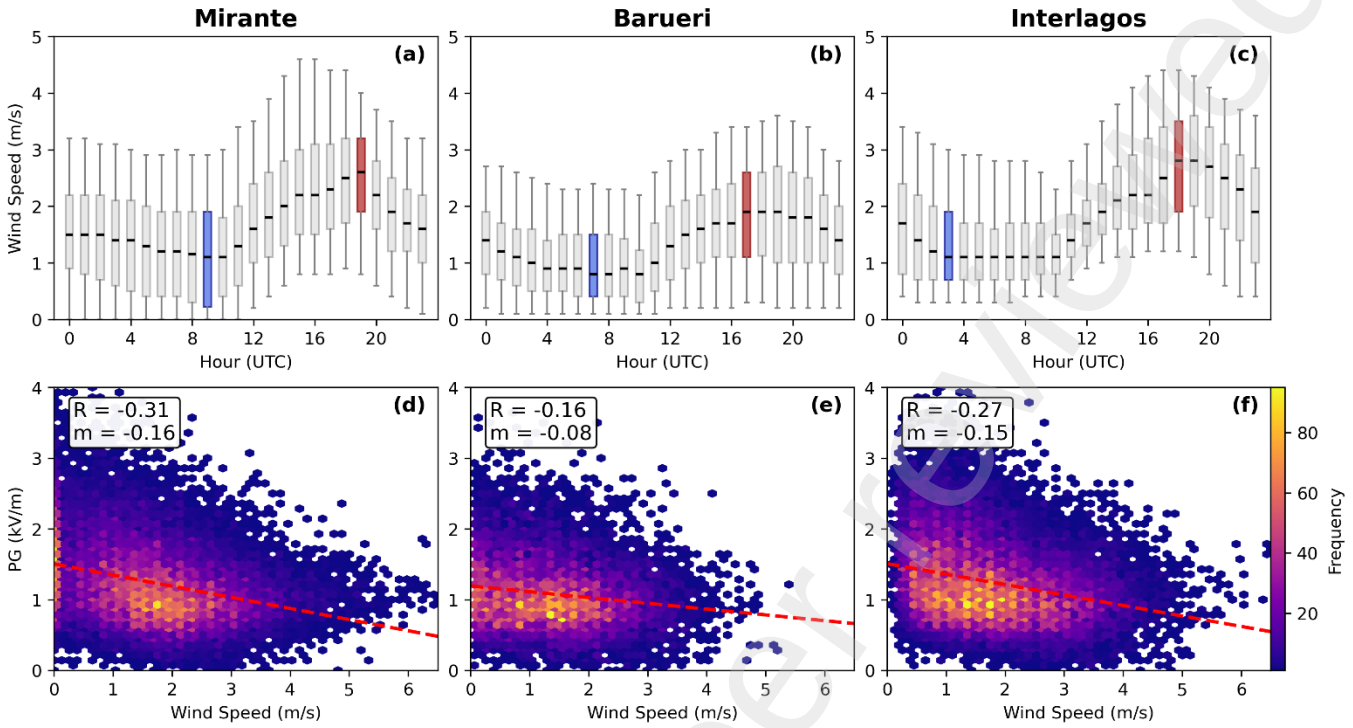

Figure 6. Top: Hourly distribution of wind speed for the Mirante, Interlagos, and Barueri meteorological stations from 2018 to 2024, shown as boxplots (boxes indicate the interquartile range and the central line denotes the median). Bottom: Hexbin density plots showing the relationship between hourly wind speed and PG for each of the three stations.

To go further in the temporal analysis, we examined wind direction because, beyond wind speed, the direction controls the origin of air masses and the effectiveness of ventilation, thereby modulating both pollutant removal and the PG. **Figure 7** shows that the relationship between wind speed, pollutants, and PG varies according to the main ventilation regime in São Paulo. The strongest negative correlations occur under southerly to southwesterly winds, especially at Mirante (NO_2 r = −0.61; NOx r = −0.57; PG r = −0.41), which are typically associated with synoptic post-frontal inflows that bring clean maritime air and enhanced turbulence (Ribeiro et al., 2018). At Interlagos, the largest anticorrelations appear for southerly and southeasterly sectors, in agreement with the influence of the sea-breeze system entering from the Atlantic Ocean. When the three stations are averaged, an E–SE–S–SW regime (r ≈ −0.4 to −0.46 for NOx and r ≈ −0.25 to −0.35 for PG) emerges as the dominant driver of pollutant removal and PG modulation. This coherent spatial pattern across the metropolitan area confirms that, even under low-wind fair-weather conditions, directional ventilation produced by sea-breeze inflow and southern frontal activity is the main mechanism linking air quality and atmospheric electrification.

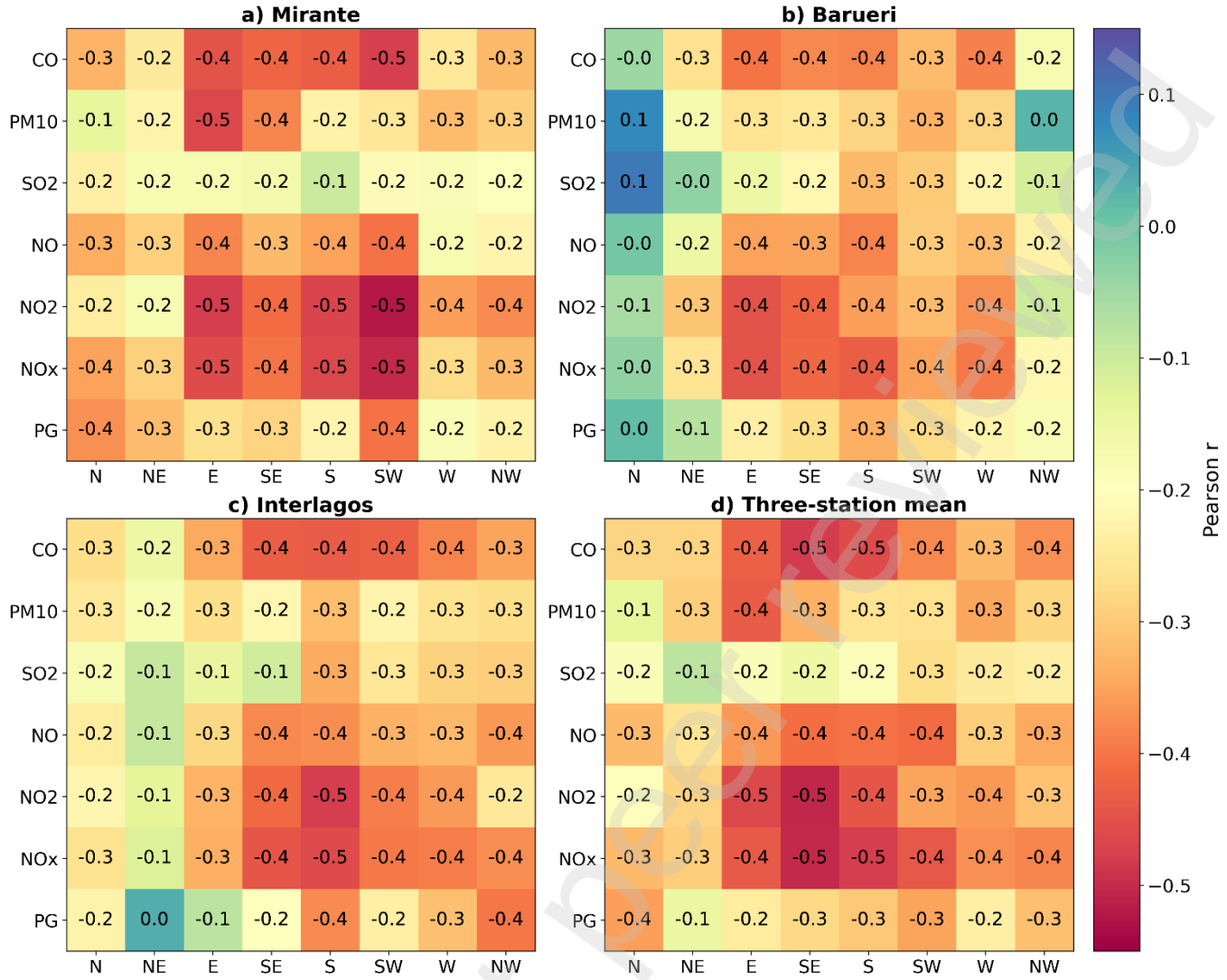

Figure 7. Pearson correlation coefficients (r) between wind speed and pollutants (CO, PM_{10}, SO_2, NO, NO_2, NOx) and PG, computed by 45° wind sectors for Mirante, Barueri, and Interlagos, and for the three-station regional mean.

Although wind speed exerts a physically consistent damping effect on the PG **diurnal variation** through enhanced turbulent mixing, the relatively weak correlation magnitudes observed within the accepted fair-weather wind regime confirm that wind speed alone cannot account for the observed PG–pollutant coupling patterns. This result validates the adopted fair-weather classification and motivates the subsequent analysis of the electrical baseline and pollutant-related modulation of PG presented in Sections 4.2 and 4.3.

4.2 Fair-weather electrical baseline in São Paulo

Under FW conditions, the PG in São Paulo exhibits a well-defined diurnal structure that departs markedly from the canonical global behavior (the Carnegie curve). Figure 8 summarizes the mean fair-weather diurnal cycle of the PG, shown as (a) the annual mean cycle and (b) the seasonal mean cycles. To represent climatological variability rather than short-term noise, the PG diurnal curve was first computed independently for each month. Then, the annual and seasonal hourly mean and ±1σ (σ is the standard deviation) envelope were derived across the ensemble of monthly diurnal cycles. For reference, the canonical Carnegie curve is also included in panel (a) as a dashed line, after linear rescaling to match the mean level and diurnal amplitude of the São Paulo annual fair-weather cycle. This scaling preserves the phase and shape of the Carnegie variation while allowing a direct visual comparison of the diurnal structure, rather than its absolute magnitude.

The annual fair-weather cycle displays a pronounced morning enhancement, with a clear maximum at 11 UTC (08 LT), where PG reaches approximately 1.64 kV m^{-1}. The lowest values occur in the early morning around 06 UTC (03 LT) (~1.06 kV m^{-1}), followed by a gradual recovery. During the late afternoon (≈17–19 UTC; 14–16 LT), PG values decrease again, forming a broad and shallow depression with weak local minima (~1.10–1.11 kV m^{-1}), coincident with the period of strongest boundary-layer mixing (Moreira et al., 2024).

This diurnal structure differs in both phase and shape from the canonical Carnegie curve, which typically exhibits a global maximum near 19–20 UTC and a minimum close to 03 UTC. Seasonally, the phase of the PG cycle is preserved, but its amplitude varies substantially. The relative diurnal amplitude, quantified as (max–min)/mean, ranges from ~47% on an annual basis to ~56–57% during summer (DJF) and winter (JJA). Winter (JJA) exhibits the largest absolute PG values and the strongest day–night contrasts, consistent with enhanced stability and charge accumulation, whereas summer (DJF) displays similarly large relative amplitudes despite lower mean PG values, reflecting strong diurnal modulation under convective daytime mixing. This baseline defines the fair-weather electrical state used to contextualize the PG–pollutant coupling and event-related departures examined in the following sections.

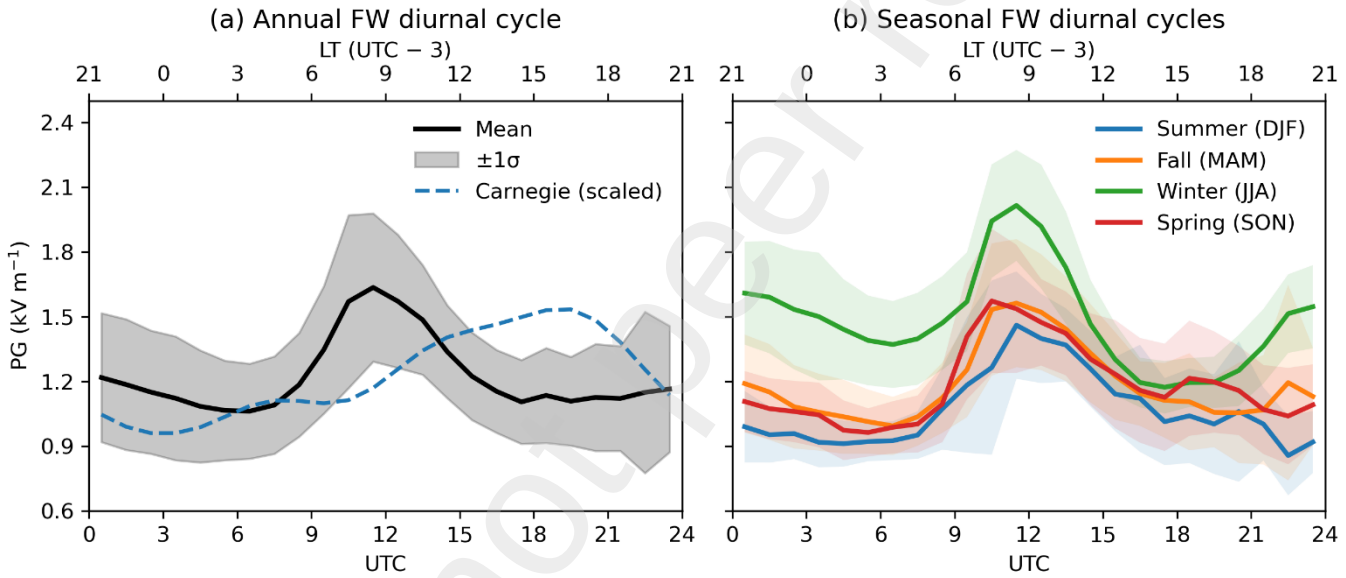

Figure 8. Fair-weather diurnal cycle of the atmospheric potential gradient (PG) in São Paulo: (a) annual mean and (b) seasonal means. Shading indicates the ±1σ envelope (σ denotes the standard deviation), computed across the ensemble of monthly diurnal curves. In panel (a), the canonical Carnegie curve is included as a dashed line for reference.

4.3 Variability of PG–Pollutant Correlations

The analysis of the 89 strict simultaneous days reveals a clear and consistent hierarchy in the strength of the PG–pollutant association (Figure 9, top row). For each retained day (≥20 valid hours), correlation coefficients are computed from the corresponding intra-day (hourly) PG and pollutant time series, and Figure 9 summarizes the distribution of these daily correlation values. Both Pearson (r) and Spearman (ρ) correlation coefficients show approximately similar values, indicating that the inferred hierarchy is robust with respect to the choice of correlation metric. Primary combustion-related gases, namely NOx, CO, and NO, exhibit the strongest coupling with PG, with median Spearman coefficients on the order of $\rho \approx 0.6$, with the majority of daily correlations being statistically significant ($p < 0.05$). Sulfur dioxide (SO_2) displays comparable rank-based correlations, clustering with the combustion group under stable fair-weather conditions.

Particulate matter (PM10) consistently ranks below the primary gaseous pollutants. Although its median Pearson correlation **coefficient** can approach that of some gases, its **median** Spearman correlation **coefficient** remains distinctly lower, reflecting a weaker and more regime-dependent association with PG. For the strictly simultaneous subset (Figure 9, top row), NO_2 exhibits relatively low median correlation values compared to other primary gases. Overall, this hierarchy indicates that near-surface PG is most sensitive to combustion-related gaseous pollutants, while PM10 displays a more variable and regime-dependent relationship.

To evaluate the robustness of this hierarchy, the analysis was repeated using all available days, defined as days meeting the same daily completeness criterion (≥20 valid hourly measurements) but without requiring full inter-pollutant simultaneity. This substantially increases data availability, yielding approximately 170 to 490 valid days per pollutant (Figure 9, bottom row). While median correlation values decrease slightly when compared to the strictly simultaneous subset, the inter-pollutant ranking and the overall distributional structure remain largely preserved. Notably, under this expanded dataset, NO_2 emerges among the top-ranked species in terms of median correlation strength, indicating that its apparent weakness in the high-confidence subset reflects sampling constraints rather than an intrinsically weak PG–NO_2 coupling. This confirms that the observed hierarchy is not an artifact of the simultaneity requirement imposed on the high-confidence dataset, but represents a stable feature of PG–pollutant coupling in São Paulo.

Beyond the median behavior, the boxplot distributions in Figure 9 reveal broad and asymmetric PG–pollutant correlation ranges for all species. For both Pearson and Spearman **correlation coeficients**, interquartile ranges extend from moderate to high correlation values, with correlation coefficients exceeding 0.8 forming a continuous extension of the observed distributions rather than isolated statistical outliers. For all pollutants, including PM_{10}, maximum Pearson and Spearman correlation **coefficients** reach values of approximately 0.9–0.95. This behavior is preserved when considering all available days, despite a modest reduction in median values, indicating that the distributional structure of PG–pollutant coupling is robust to dataset selection and filtering criteria. In contrast to gaseous pollutants, PM_{10} distributions exhibit pronounced asymmetry, with extended negative tails coexisting with high positive correlation values, reflecting a substantially larger variability range in daily PG–PM_{10} coupling. This reduced distributional coherence indicates a more regime-dependent and less uniform coupling with PG compared to primary combustion-related gases, consistent with the influence of multiple, competing processes affecting PM_{10} variability across different dynamical conditions.

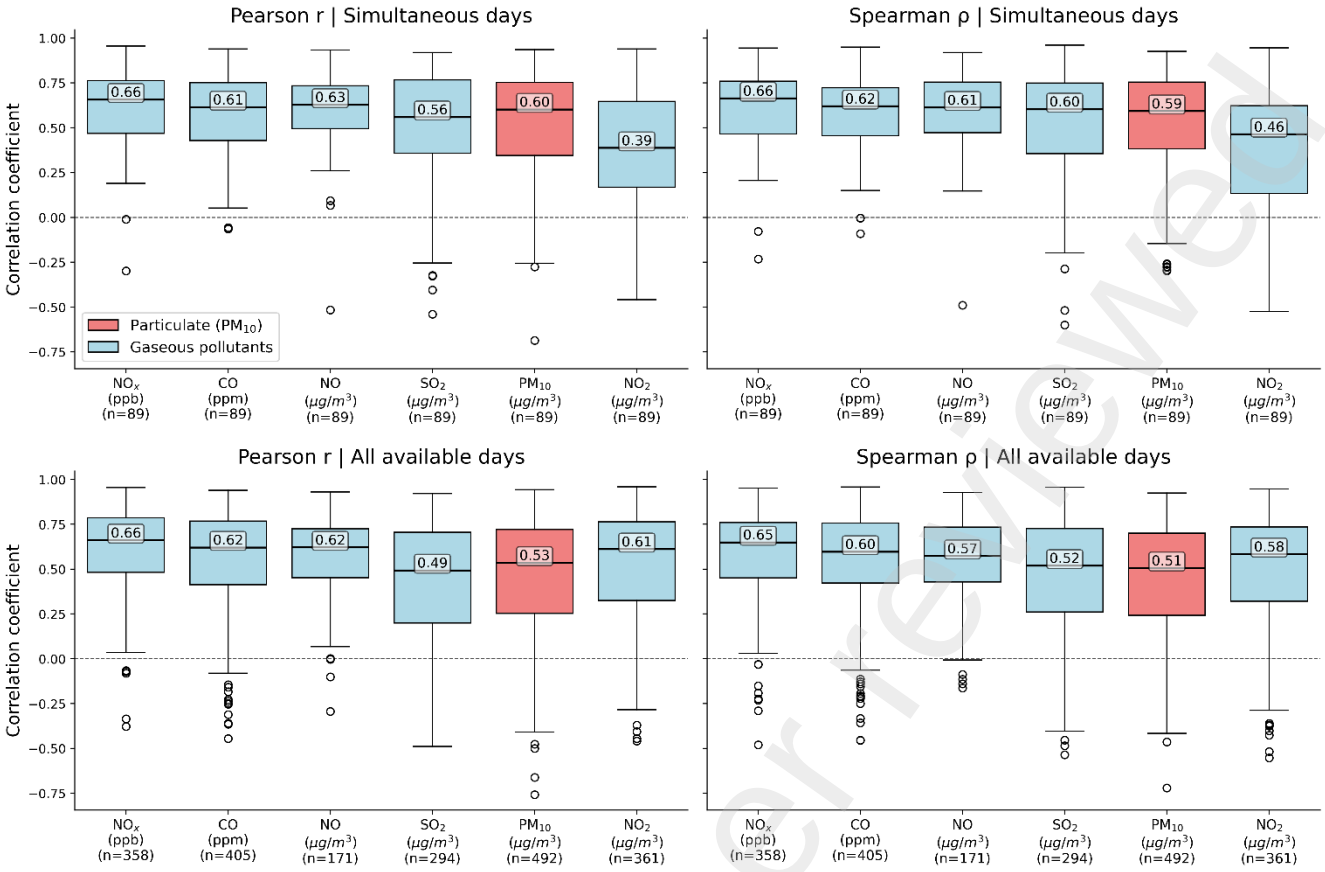

Figure 9. Boxplot distributions of daily Pearson *r* and Spearman *ρ* correlation coefficients between PG and air pollutants. Top row: simultaneous days. Bottom row: all available days. PM_{10} is highlighted in red.

Beyond this general ranking, the strength of the PG-pollutant coupling exhibits a robust diurnal pattern for all pollutants **(Figure 10).** The correlation is consistently strong during nighttime and early morning hours (typically 0.5 to 0.7) but systematically weakens after noon, reaching a distinct minimum in the late afternoon between 12:00 and 17:00 LT. This period of decoupling aligns perfectly with the expected daily evolution of the atmospheric boundary layer. The combination of maximum convective activity and peak wind speeds (as shown in **Figure 4**) enhances vertical mixing, diluting surface pollutants into a deeper layer and thus weakening their measured association with near-surface PG.

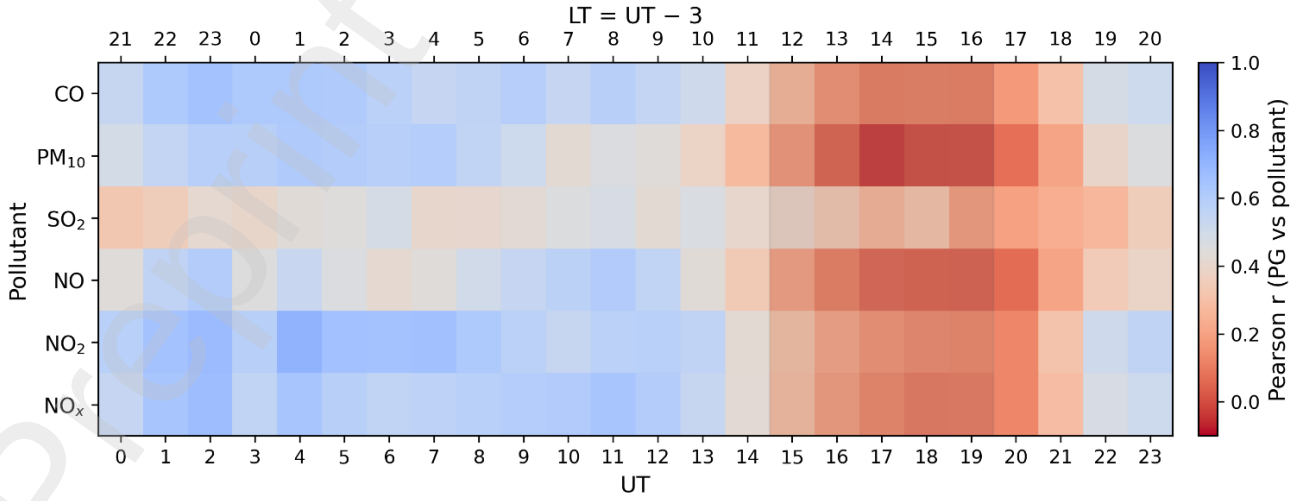

Figure 10. Diurnal cycle of PG–pollutant correlations (Pearson R) under fair-weather conditions. The top axis shows Local Time (LT = UTC-3). Warm colors (red tones) correspond to low correlation values (R ≈ 0), which dominate during the afternoon period (12:00–17:00 LT), coincident with maximum turbulent mixing.

A direct comparison between Pearson **(r)** and Spearman **(ρ)** correlation coefficients indicates that the observed diurnal patterns are robust with respect to the choice of correlation metric. Differences between r and ρ are generally small (mean $|r - \rho| \approx 0.03$), with Spearman coefficients being slightly higher in most cases, consistent with predominantly monotonic but not strictly linear relationships. Changes in correlation sign between the two metrics are rare and occur only when correlations are close to zero, indicating no qualitative inconsistency. On this basis, Pearson correlations are used to summarize the seasonal modulation without loss of generality. Pearson correlation p-values computed from the underlying hourly data indicate that most PG–pollutant correlations are statistically significant ($p < 0.05$), with non-significant cases primarily confined to regimes where correlation magnitudes are close to zero (e.g., Spring afternoon conditions). In addition to the diurnal modulation described above, the PG–pollutant relationship exhibits a clear seasonal dependence when stratified jointly by season and diurnal regime, as summarized in Figure 11.

Pearson correlation coefficients are strongest during Winter and Fall nights (00–05 UTC; 21–02 LT) across most pollutants, including PM_{10}, NO_x, NO, and CO, indicating enhanced sensitivity of PG to near-surface pollutant variability under dynamically stable atmospheric conditions. Among the remaining seasons, nocturnal correlations are weakest in Summer, reflecting reduced PG–pollutant coherence even during nighttime regimes. In contrast, the weakest correlations across all seasons and pollutants occur during Spring afternoons (15–20 UTC; 12–17 LT), when several species exhibit near-zero or negative values, consistent with strong convective mixing and partial decoupling between surface pollutant concentrations and PG variability. Spring is characterized by intermediate nocturnal correlations combined with pronounced daytime degradation, while Fall maintains a comparatively strong coupling across both diurnal windows. These results highlight the non-stationary nature of PG–pollutant correlations and emphasize the need to interpret them within a combined seasonal and diurnal regime framework.

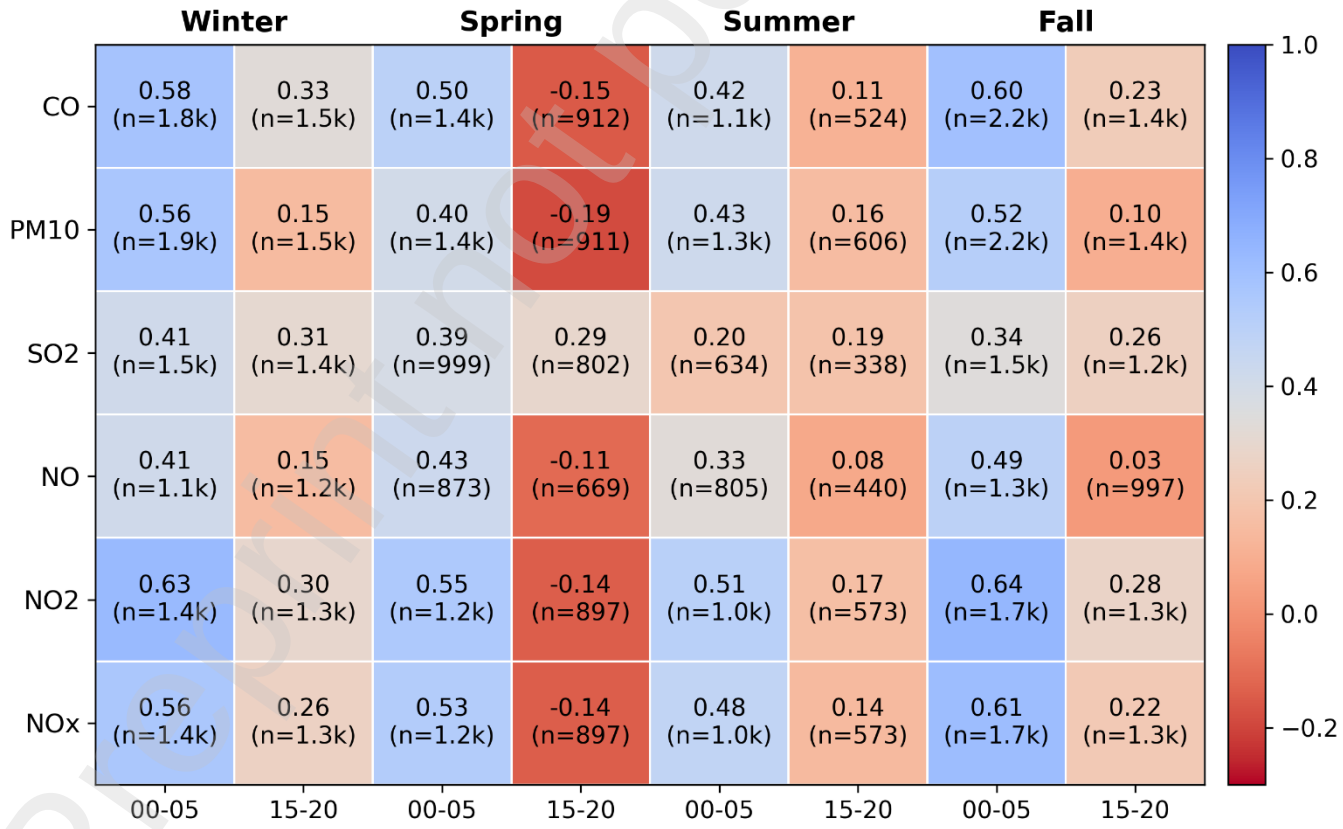

Figure 11. Seasonal–diurnal heatmap of Pearson correlation coefficients (r) between FW PG and hourly concentrations of CO, NO, NO_2, NO_x, PM_{10}, and SO_2 in São Paulo (2018–2024). Columns are grouped by season (DJF, MAM, JJA, SON) and by two diurnal windows (00–05 UTC and 15–20 UTC). Numbers in parentheses indicate the number of paired hourly samples (n).

4.4 Temporal Dynamics and Lag Analysis

The cross-correlation analysis of the 168-hour weekly profiles reveals distinct temporal relationships between the PG and urban pollutants, as illustrated in **Figure 12** and summarized in **Table 1.** In addition to lag correlations, we report the Trend Match (TM) index to quantify the percentage of synchronized directional changes (first differences) between the series (Yaniv et al., 2026).

Nitrogen oxides (NOx) and carbon monoxide (CO) exhibit the highest degree of synchronicity, with maximum Pearson correlation coefficients of r = 0.926 and 0.827, respectively, both occurring at zero lag. These temporal alignments suggest differing response times, but should be interpreted as indicative rather than mechanistic, given the hourly resolution. Nitric oxide (NO) also displays a strong association (r = 0.856), but with a negative temporal shift, reaching its peak correlation at a −1 hour lag.

In contrast, pollutants associated with secondary formation processes or larger particle sizes show positive temporal shifts relative to the PG. Nitrogen dioxide (NO_2) peaks with a +1 hour lag (r = 0.806), while PM_{10} exhibits a correlation of r = 0.756, also at a +1 hour lag.

Although the Trend Match Index for PM_{10} (60.5%) is lower than that of primary gases such as CO (80.2%) or NOx (77.3%), it remains well above random expectation and is associated with a clearly defined correlation maximum at a +1 hour lag, indicating a coherent but more delayed coupling between PG and particulate matter compared to gaseous species.

Overall, these results indicate a clear hierarchy of temporal responses, in which primary gaseous emissions show immediate or leading associations with the PG, whereas secondary gases and particulates exhibit a delayed alignment with the PG.

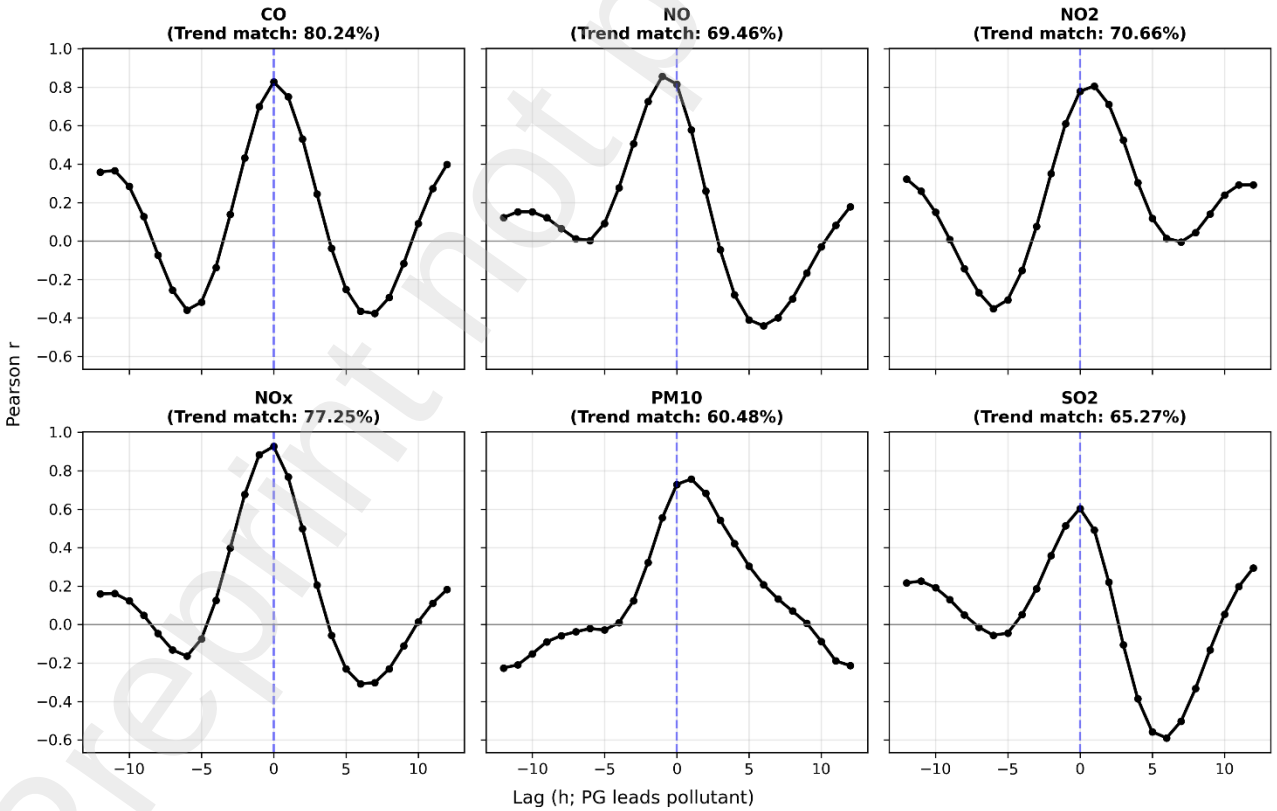

Figure. 12. Cross-correlation (lag relationship) analysis between the PG and six key urban pollutants (NOx, NO, CO, NO2, PM10, and SO2) in São Paulo. The analysis is based on a 168-hour weekly average profile to eliminate transient meteorological noise. Positive lags indicate that the pollutant concentration peaks after the PG response.

Table 1. Summary of peak correlations, temporal lags and Trend Match values (%) for urban pollutants in São Paulo.

Pollutant	Peak r	Lag (h)	TM (%)
NOx	0.926	0	77
NO	0.857	−1	69
CO	0.827	0	80
NO_2	0.806	+1	71
PM_{10}	0.757	+1	60
SO_2	0.604	0	65

4.5 Wind-speed–dependent modulation of PG–pollutant correlations

While Sections 4.1–4.3 established the temporal, directional, and seasonal variability of PG–pollutant coupling under fair-weather conditions, an additional analysis was conducted to quantify the modulation of this relationship by wind speed within the accepted fair-weather regime. Pearson correlation coefficients between the surface PG and individual pollutants were computed using hourly data grouped into 0.5 m s^{-1} wind-speed bins and evaluated separately for summer (DJF) and winter (JJA). For each wind-speed bin, a single correlation coefficient was calculated using all paired hourly PG–pollutant observations falling within that bin, rather than averaging or aggregating multiple correlation estimates.

Figure 13 summarizes the resulting wind-speed dependence of the PG–pollutant correlations. Wind speed is defined as the regional mean of the Mirante, Interlagos, and Barueri stations, and only the 0–4 m s^{-1} range is shown, which encompasses the vast majority of fair-weather observations. Bins with fewer than 50 paired hourly samples for a given pollutant are masked (NaN).

Across both seasons, the strongest PG–pollutant correlations occur under weak wind conditions, typically below ~1.5 m s^{-1}. Correlation magnitudes generally decrease with increasing wind speed for most pollutants, indicating a systematic weakening of the coupling between near-surface pollutant concentrations and the PG. This decay becomes evident at intermediate wind speeds (~2.5–3.0 m s^{-1}) and continues toward higher values.

A clear seasonal contrast is observed. In summer (DJF), correlations weaken rapidly with increasing wind speed and approach near-zero values by ~3.0–3.5 m s^{-1} for most pollutants. In winter (JJA), correlations are systematically stronger at low wind speeds and remain weak but non-zero over a wider wind-speed range, in several cases extending up to ~3.5–4.0 m s^{-1}.

A markedly different behavior is observed for PM_{10} (used here as a proxy for coarse-mode particles). Correlations decrease more abruptly with increasing wind speed than those of gaseous species. In summer, PG–PM_{10} correlations weaken sharply and approach near-zero values by ~3.0–3.5 m s^{-1}. In winter, positive correlations observed at low and moderate wind speeds collapse near ~2.5–3.0 m s^{-1} and reverse sign in the 3.5–4.0 m s^{-1} bin, where a negative correlation emerges. While some gaseous species (e.g., NO_2 and NOx) also approach near-zero correlations at high wind speeds, no comparable sign reversal is detected for the gaseous pollutants.

To assess whether this behavior is driven by episodic events, the temporal distribution of observations within each wind-speed bin was examined. For the critical 3.5–4.0 m s^{-1} bin, observations are distributed across 48 distinct summer days and 51 distinct winter days, with typically only 1–3 hours contributing per day, indicating a recurrent and systematic pattern rather than isolated events.

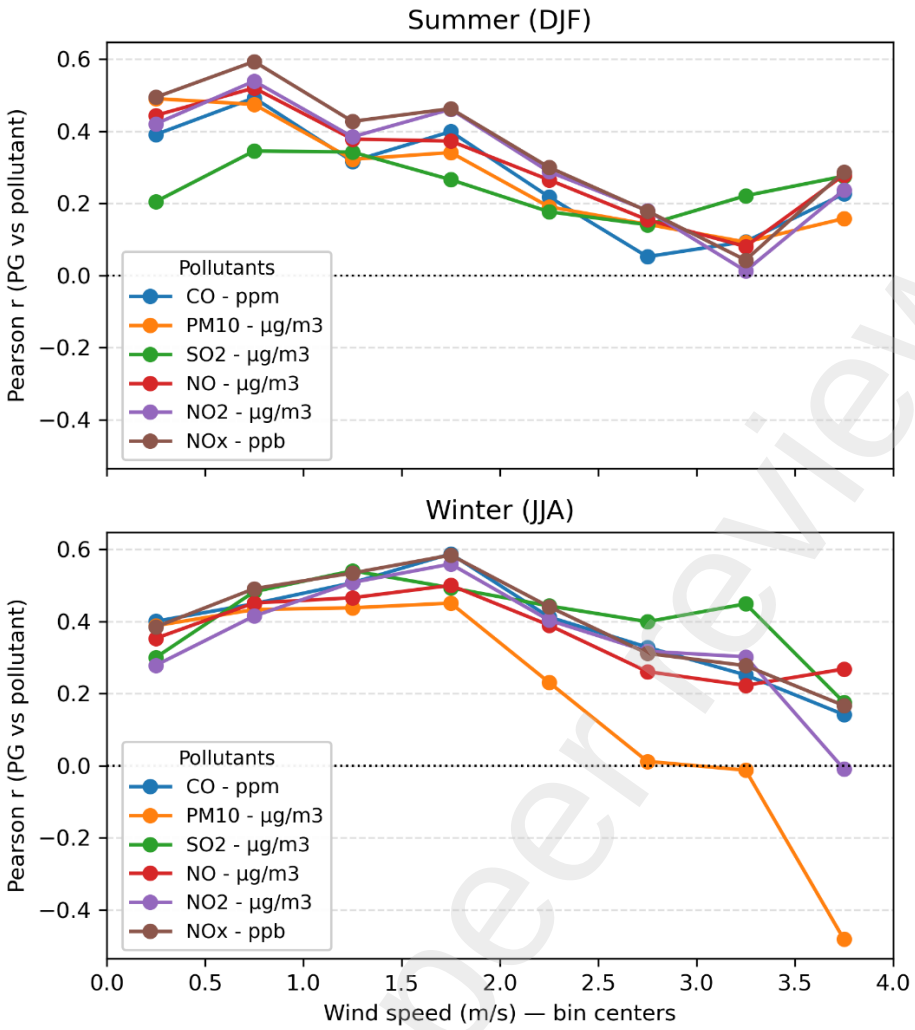

Figure 13. Wind-speed dependence of hourly PG–pollutant Pearson correlation coefficients under fair-weather conditions in São Paulo (2018–2024), shown for summer (DJF) and winter (JJA). Each point represents a single correlation coefficient computed from all paired hourly data within the corresponding wind-speed bin.

Overall, these results reveal a clear wind-speed–dependent modulation of the PG–pollutant relationship within FW conditions. While wind speed does not act as a primary driver of PG variability, it systematically weakens the coupling between PG and pollutants, with PM_{10} exhibiting a sharper and more seasonally dependent response than gaseous species

4.6 Case studies of meteorological modulation

To better understand the drivers behind the variability observed in Section 4.3, selected days with exceptionally high or low correlations were analyzed in detail. These case studies illustrate how atmospheric conditions modulate the PG–pollutant relationship beyond the statistical aggregates.

Figure 14 shows a representative wintertime case (18 July 2024) characterized by cloud-free conditions and weak surface winds, which allows a clear assessment of PG behavior under fair-weather conditions. Throughout the day, the observed PG remains systematically higher than the winter fair-weather climatological mean, with positive anomalies reaching up to approximately +1.2 kV m^{-1} during nighttime and early morning hours. This deviation persists for several consecutive hours, indicating a sustained anomaly rather than short-lived fluctuations.

Notably, between 00 and 09 UT, both PG and PM_{10} remain well above the seasonal fair-weather variability envelope, exceeding the climatological mean by more than one standard deviation for prolonged periods. This simultaneous exceedance of the ±1σ range indicates that the observed enhancement cannot be attributed to typical day-to-day variability within the winter season.

During this period, PG and PM_{10} exhibit a very strong positive temporal correlation (Pearson r = 0.93), indicating a tightly coupled response under dynamically stable conditions. Simultaneously, PM_{10} concentrations remain elevated during periods of enhanced PG, particularly under stable nocturnal conditions.

The lower panel of **Figure 14** confirms that these prolonged PG and PM_{10} enhancements occur under cloud-free conditions and persistently weak winds, minimizing the influence of convection, precipitation, and strong mechanical turbulence. Short-lived wind speed fluctuations do not coincide with abrupt PG changes, indicating limited sensitivity to transient dynamical forcing during this event.

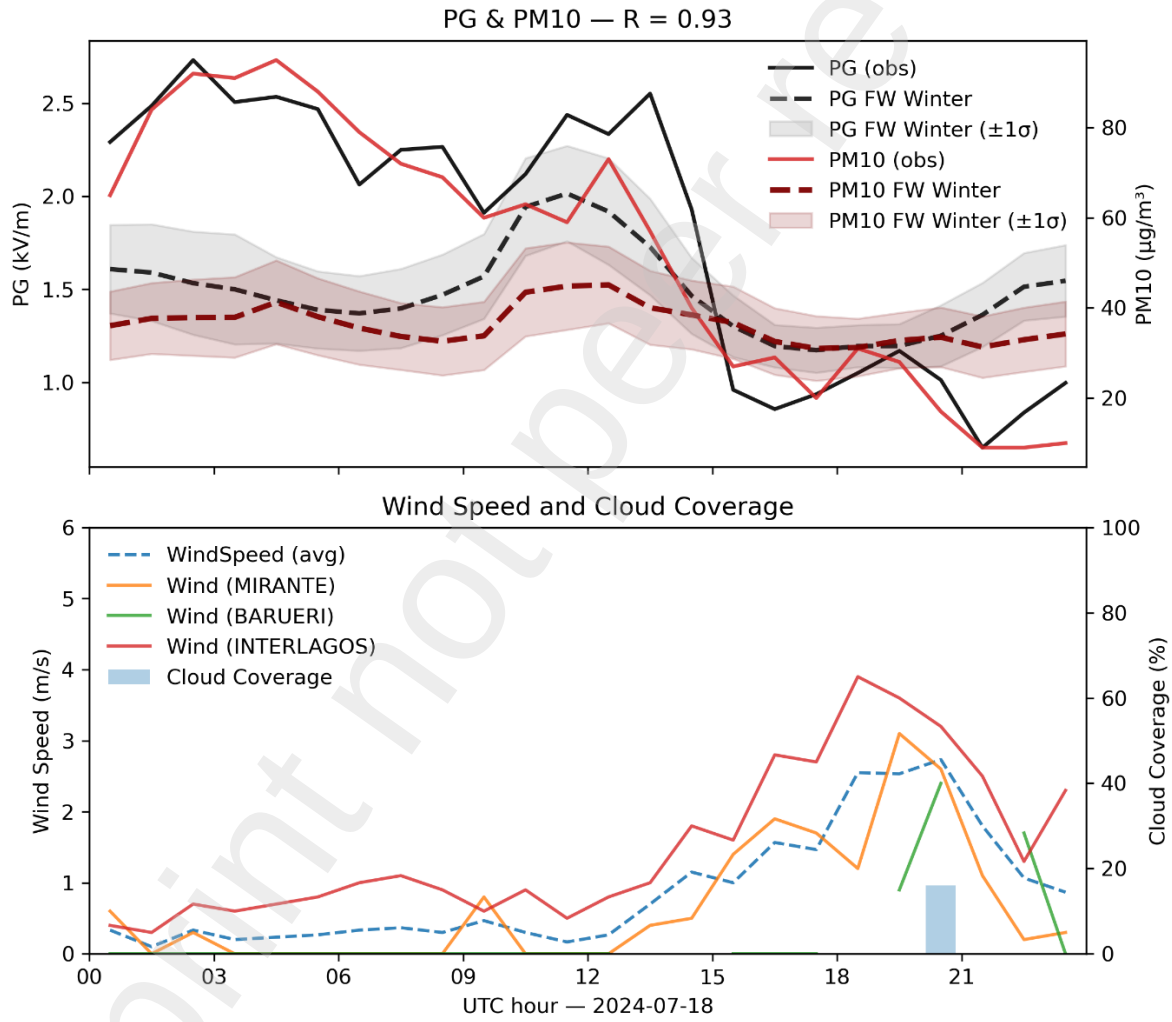

Figure 14. Hourly evolution of observed PG and PM_{10} on 18 July 2024, shown together with the winter fair-weather climatology (mean ±1σ). The lower panel displays the corresponding mean wind speed and satellite-derived cloud coverage, highlighting a cloud-free, weak-wind regime.

Figure 15 extends this analysis by contrasting a perturbed day (May 20th, 2018) and two fair-weather days (May 21th and May 22th, 2018) characterized by similarly clear skies but markedly different dynamical regimes. On 20 May, persistently strong winds dominate throughout the day, and both PG and PM_{10} remain systematically below the winter fair-weather climatology, frequently falling below the −1σ threshold.

The intervening day (21 May) represents a transition between regimes, with decreasing wind speeds and a gradual recovery of both PG and pollutant concentrations toward climatological values.

In contrast, 22 May is characterized by weak wind conditions, during which both PG and PM_{10} increase substantially and remain above the +1σ level for most of the day, exhibiting pronounced temporal co-variability.

Despite comparable cloud-free conditions, these three consecutive days display fundamentally different PG responses, highlighting the sensitivity of near-surface atmospheric electricity to the combined effects of aerosol loading and boundary-layer dynamics. When considering the full 20–22 May period, PG and PM_{10} exhibit a high positive correlation (Pearson r = 0.87), driven primarily by the dynamically stable conditions on 22 May.

Overall, these case studies demonstrate that strong daily-scale PG–pollutant correlations preferentially emerge under weak-wind, dynamically stable fair-weather conditions, whereas enhanced mechanical mixing can suppress coherent electric-field responses even in the presence of measurable aerosol concentrations. The broader implications of this regime dependence are discussed in Section 5.

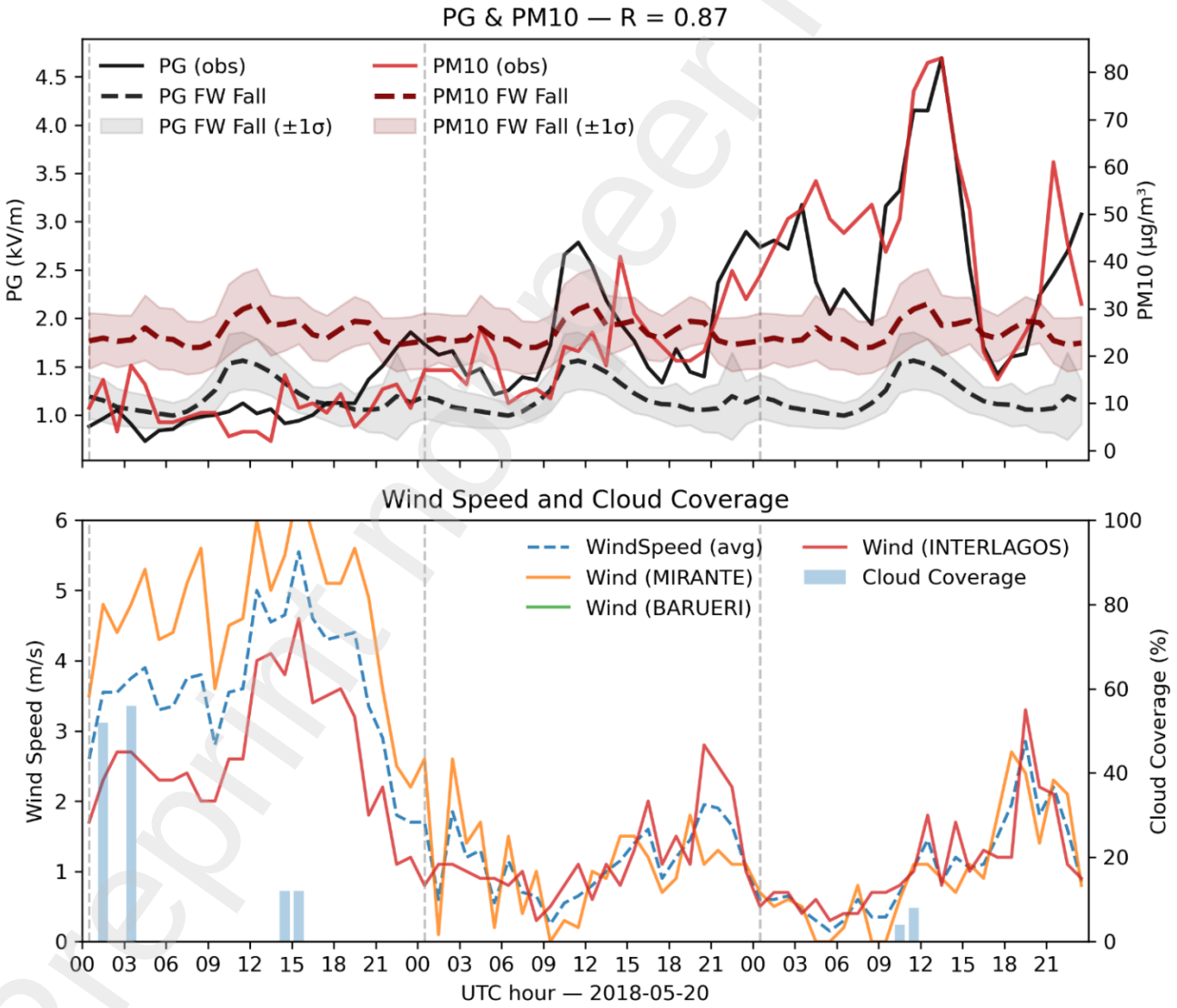

Figure 15. Hourly evolution of observed PG and PM_{10} during two fair-weather days (20–22 May 2018), shown relative to the winter fair-weather climatology (mean ±1σ). The lower panel displays the corresponding mean wind speed and satellite-derived cloud coverage. Despite similarly cloud-free conditions, contrasting wind regimes lead to markedly different PG–pollutant coupling.

4.7 Anthropogenic Perturbations

To assess the sensitivity of the PG to changes in anthropogenic emissions, three complementary perturbation regimes were examined. First, the systematic modulation associated with the weekly activity cycle was analyzed by contrasting weekdays and weekends. This recurrent pattern provides a baseline representation of anthropogenic influence under normal operating conditions. In addition, two major episodes of abrupt emission reductions were investigated separately: the truckers' strike in May 2018 and the COVID-19 lockdown in 2020. Both events produced sharp, externally forced disruptions to traffic and industrial activity, offering natural experiments to test the response of PG to rapid decreases in anthropogenic emissions. PG behavior during these perturbations was evaluated relative to reference periods to quantify the magnitude and persistence of any associated anomalies.

4.7.1 Weekday–weekend modulation

Figure 16 shows the weekday–weekend modulation of the PG under fair-weather conditions, expressed as the mean hourly difference between working days and weekends. Systematic differences are observed across the diurnal cycle, with PG generally exhibiting higher values during weekdays than during weekends. The magnitude of these anomalies remains small relative to the absolute PG levels and varies with both local time and season, characterizing the typical range of weekday–weekend variability in the urban PG record.

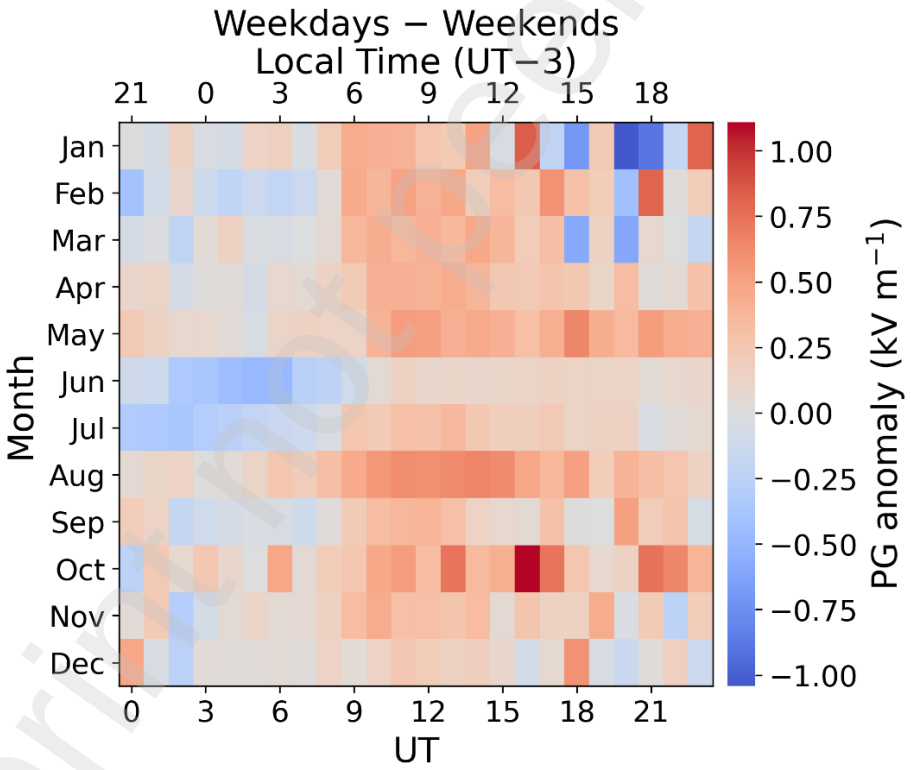

Figure 16. Heat map of the mean hourly weekday–weekend PG anomaly (WD − WE) under fair-weather conditions as a function of month and universal time (UTC). The upper axis indicates local time (UTC−3).

4.7.2. Truckers' strike (May 2018)

In May 2018, a truck-driver strike in São Paulo provided conditions for conducting a real-world experiment on the relationship between vehicle emissions, air quality, and public health (Leirião et al., 2020), as well as other less-explored phenomena such as the interplay between PG and air pollution. **Figure 17** illustrates the temporal evolution of the near-surface PG and selected traffic-related pollutants across the strike.

A short-lived increase in PG is observed at the onset of the strike; however, this anomaly is not sustained throughout the perturbation period and remains comparable to the baseline variability observed during the preceding weeks. Concurrent reductions in NO_x and CO concentrations are modest and intermittent, indicating that the decrease in anthropogenic emissions was limited in magnitude and duration. Overall, the strike did not produce a persistent or statistically distinct departure of PG from its pre-event range, suggesting that this perturbation was insufficient to induce a robust modification of the PG under fair-weather conditions.

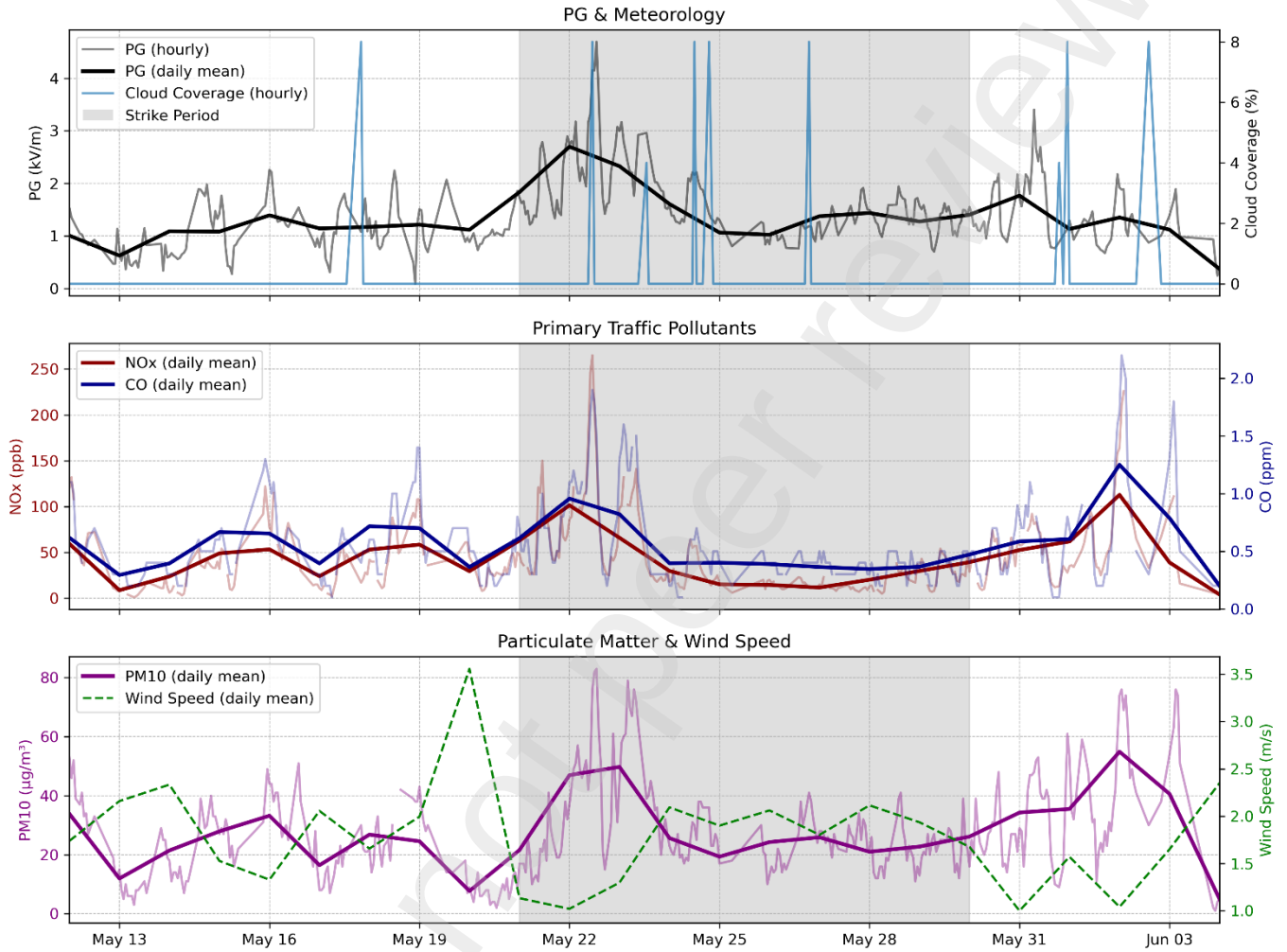

Figure 17. Temporal evolution of the near-surface PG and selected atmospheric and anthropogenic variables during the May 2018 truckers' strike in São Paulo. The upper panel shows hourly PG (gray) and its daily mean (black), together with satellite-derived cloud coverage. The middle panel presents daily mean concentrations of primary traffic-related pollutants (NO_x and CO). The lower panel displays daily mean PM_{10} concentrations and wind speed as indicators of aerosol loading and mechanical mixing. The shaded area denotes the strike period.

4.7.3 COVID-19 lockdown (2020)

The COVID-19 lockdown in 2020 constitutes the most pronounced anthropogenic perturbation examined in this study. Satellite data revealed that up to 57% of the state of São Paulo exhibited reductions in tropospheric NO_2 column densities during the pandemic outbreak (Rudke et al., 2023). **Figure 18** compares the fair-weather diurnal PG curves for individual years computed over the March–May window (15 March–15 May) against the annual fair-weather baseline defined in Section 4.2 and shown in Fig. 8a. Among all years analyzed, 2020 exhibits the lowest PG values across the entire diurnal cycle.

Relative to the annual mean diurnal curve, the 2020 PG profile is systematically shifted toward lower values while preserving the characteristic diurnal structure of fair-weather conditions in São Paulo. The reduction is coherent across all hours and frequently exceeds the −1σ envelope of the multi-year annual baseline, indicating a sustained anomaly rather than hour-specific deviations.

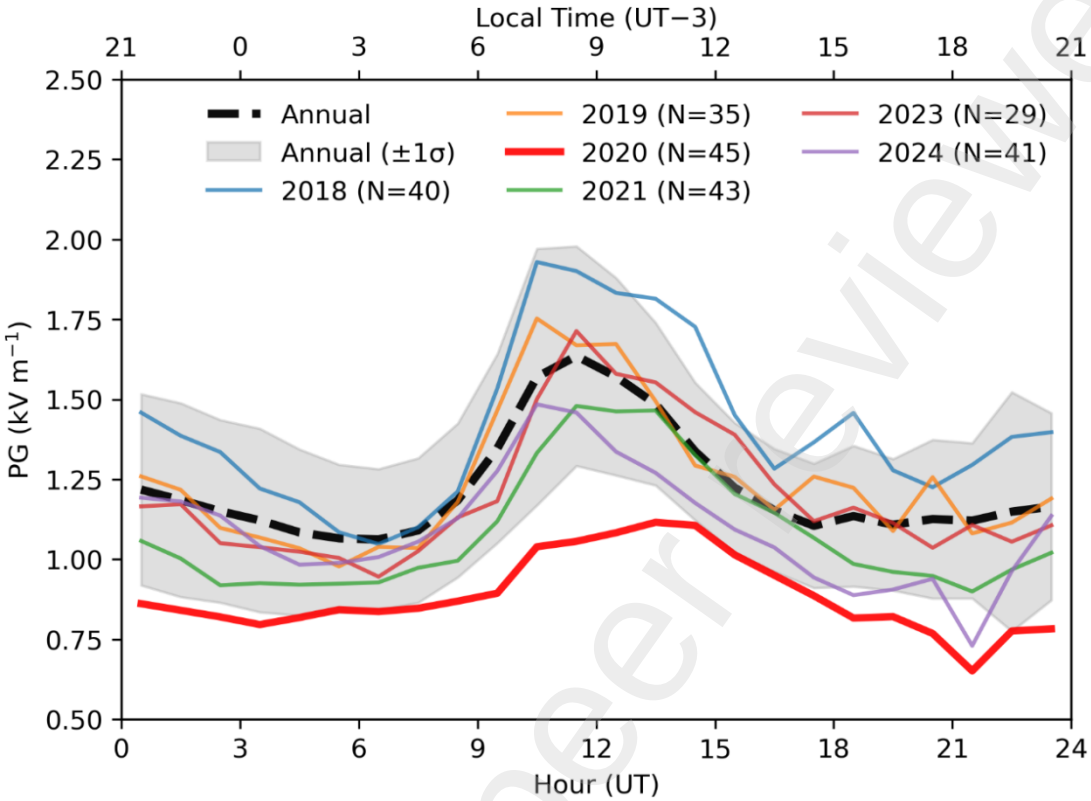

Figure 18. Fair-weather diurnal PG curves for 2018–2024 computed over 15 March–15 May. Colored lines show year-specific diurnal means (mid-hour UTC), with the number of fair-weather day-equivalents (N) indicated in the legend. The dashed black line and gray shading represent the annual fair-weather baseline (mean ±1σ) defined in Fig. 8a.

This behavior cannot be attributed to data-availability bias. On the contrary, 2020 presents one of the highest numbers of fair-weather observations within the March–May window (~45 day-equivalents), including near-complete coverage during April. Despite this extensive sampling, PG values remain consistently lower than those observed in pre- and post-pandemic years. In contrast to the short-lived response observed during the May 2018 truckers' strike, the COVID-19 lockdown is associated with a persistent and statistically robust reduction in fair-weather PG. A complementary qualitative analysis at a low-emission site (Ica, Peru) is included in Appendix B for contextual comparison.

4.8 PG-Based Pollutant Prediction (Machine Learning)

The predictive capacity of the PG for particulate (PM_{10}) and gaseous (CO, NO_2) pollutants was evaluated using MLR and RF models under two distinct temporal regimes: Stable Night (UTC 00–12) and Full Day (UTC 00–23). These pollutants were selected to span different physical and chemical regimes, with CO representing a relatively inert primary tracer, NO_2 a reactive secondary species influenced by photochemistry, and PM_{10} a particulate component governed by additional non-electrical processes, rather than to simply target the species with the highest PG correlation. **Table 2** summarizes the model performance metrics obtained for the independent test period (2023–2024).

Target	Scenario	UTC window	Model	R^2	MAE
CO – ppm	Full Day	0–23	MLR	0.361	0.20
CO – ppm	Full Day	0–23	**RF**	**0.454**	0.18
CO – ppm	Stable Night	0–12	MLR	0.462	0.22
CO – ppm	Stable Night	0–12	RF	0.462	0.20
PM_{10} – µg m^{-3}	Full Day	0–23	MLR	0.300	12.84
PM_{10} – µg m^{-3}	Full Day	0–23	**RF**	**0.369**	12.48
PM_{10} – µg m^{-3}	Stable Night	0–12	MLR	0.458	12.41
PM_{10} – µg m^{-3}	Stable Night	0–12	RF	0.444	12.69
NO_2 – µg m^{-3}	Full Day	0–23	MLR	0.358	17.63
NO_2 – µg m^{-3}	Full Day	0–23	**RF**	**0.415**	16.62
NO_2 – µg m^{-3}	Stable Night	0–12	MLR	0.517	15.46
NO_2 – µg m^{-3}	Stable Night	0–12	RF	0.525	14.90

Table 2. MLR and RF performance metrics for CO, PM10, and NO2 under Stable Night (UTC 00–12) and Full Day (UTC 00–23) regimes during the 2023–2024 independent validation period.

Under stable nocturnal conditions (UTC 00–12), the predictive skill was consistently high across all pollutants, indicating that PG captures physically meaningful information on near-surface pollutant variability under dynamically stable fair-weather regimes. For NO_2, the highest accuracies were achieved, with the RF model reaching an R^2 of 0.53 and the MLR achieving a comparable R^2 of 0.52. Similarly, for CO and PM_{10}, both linear and non-linear models exhibited strong agreement, yielding R^2 values of approximately 0.46. Notably, the linear MLR model matched or slightly outperformed the more complex RF model for both CO and PM_{10} in this regime, indicating that, under suppressed turbulent mixing, the coupling between PG and surface pollutant accumulation is predominantly linear.

In contrast, extending the analysis to the full diurnal cycle (UTC 00–23) resulted in a pronounced degradation of predictive performance for all species. The coefficient of determination (R^2) decreased by approximately 0.10–0.15 relative to the nocturnal regime (e.g., PM_{10} MLR R^2 declined from 0.46 to 0.30). In this regime, a clear shift toward non-linear behavior was observed, with the RF model consistently outperforming the MLR (e.g., for CO, RF R^2 = 0.45 compared to MLR R^2 = 0.36). This behavior reflects the increasing complexity of interactions between PG, enhanced turbulent mixing, and photochemical processes during daytime hours, which weakens the direct electrical–pollutant coupling identified under stable conditions.

Feature importance analysis derived from the Random Forest model **(Figure 19)** further supports this interpretation. Under stable nocturnal conditions, PG emerged as the dominant predictor for all pollutants, exceeding the contribution of standard meteorological variables. The relative importance of PG was highest for gaseous pollutants (NO_2: 54.5%; CO: 46.3%) and lower for PM_{10} (39.0%), consistent with the stronger sensitivity of the PG to combustion-related emissions and near-surface conductivity changes. In all cases, the contribution of PG decreased under the Full Day scenario (e.g., NO_2 PG importance reduced to 40.5%), as meteorological drivers such as wind speed and relative humidity gained explanatory power due to enhanced convective mixing.

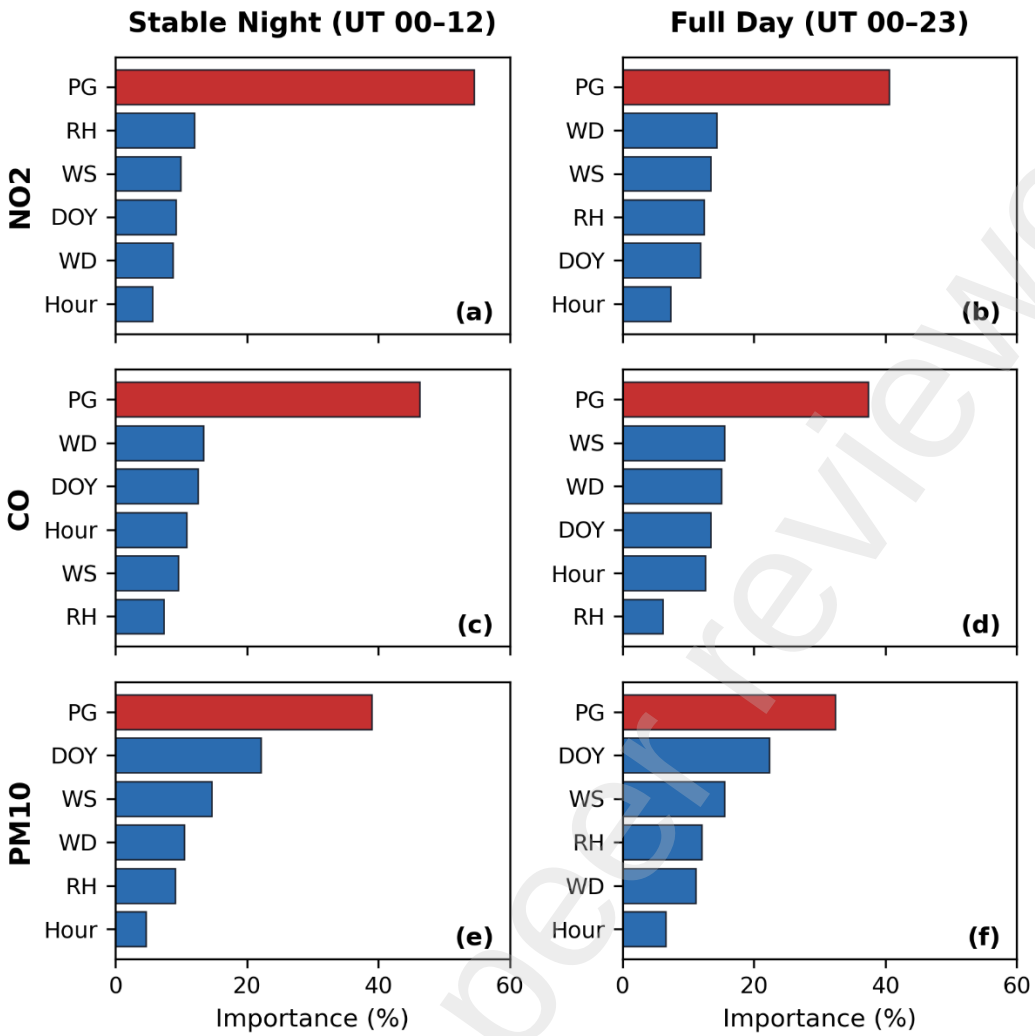

Figure 19. Random Forest features importance ranking for NO2, CO, and PM10 under two temporal regimes: (a, c, e) Stable Night (UTC 00–12) and (b, d, f) Full Day (UTC 00–23). Values indicate the percentage contribution to the total predictive error reduction.

Overall, these results demonstrate that PG is not a standalone predictor of air quality but acts as a regime-dependent electrical proxy whose predictive value is maximized under stable fair-weather conditions and systematically diminishes when boundary-layer dynamics dominate. This behavior is fully consistent with the diurnal, seasonal, and dynamical modulation of PG–pollutant coupling identified in Sections 4.2–4.6.

5. Discussion

5.1 Comparison with previous urban studies

Previous studies at urban sites including Buenos Aires, Lisbon, Reading, and more recently Tel Aviv have commonly reported stronger PG–pollutant correlations in winter than in summer, often attributing this contrast to seasonal changes in boundary-layer stability and ventilation (Harrison and Aplin, 2002; Silva et al., 2016; Velázquez et al., 2025; Yaniv et al., 2026). Our results are consistent with this seasonal ordering, with the strongest PG–pollutant coupling occurring in winter and the weakest in summer, reflecting the combined influence of strong nocturnal coupling and comparatively weaker daytime degradation. Although Winter and Fall exhibit comparable nocturnal correlation strengths, Winter maintains stronger coupling during the afternoon regime, resulting in higher seasonally averaged correlations. At the same time, earlier analyses typically relied on surface meteorological criteria and, in some cases, PG amplitude thresholds to define fair-weather conditions, which may not fully exclude thin or advected cloud fields capable of perturbing the PG.

By combining surface meteorological screening with hourly satellite-based cloud masking over a local domain, the fair-weather classification adopted here provides an electrically cleaner and more internally consistent dataset without altering the underlying seasonal structure of PG–pollutant relationships. Under this stricter filtering, the most robust and reproducible modulation emerges at the diurnal scale, with PG–pollutant coupling strengthening during nocturnal stable conditions and weakening during the afternoon mixing maximum across all seasons. In this sense, diurnal boundary-layer dynamics exert a primary control on the strength of PG–pollutant coupling, consistent with the regime-dependent role of boundary-layer structure in controlling surface–atmosphere coupling (Kotthaus et al., 2023). Seasonal differences then act primarily as a secondary modulation of this coupling amplitude through seasonally varying stability, ventilation, and wind regimes (Li et al., 2021).

This broader physical interpretation is consistent with long-term fair-weather observations at continental land stations, where reducing aerosol number concentrations modifies PG amplitudes, particularly in winter, while preserving the overall seasonal structure, indicating dominant control by boundary-layer regime and large-scale electrical forcing (Pawlak et al., 2024).

The inclusion of both trace gases and particulate matter in the São Paulo dataset further allows a clearer distinction between near-synchronous combustion markers, notably NOx and CO, and species whose coupling to PG is more regime dependent, such as PM10.

This contrast reflects the microphysical drivers of atmospheric conductivity, which is primarily reduced by the attachment of small ions to aerosol particles, a process dependent on the total particle surface area rather than mass. Harrison and Jones (2005) demonstrated that in urban environments, particle number concentrations (dominated by ultrafine particles from traffic) exhibit a significantly stronger correlation with NOx than with PM10 mass. This occurs because PM10 is gravimetrically dominated by fewer, larger particles that contribute less to the total surface area available for ion scavenging. Consequently, the strong association between PG and gaseous combustion markers observed here likely implies that NOx acts as a robust proxy for the ultrafine aerosol fraction modulating the local PG.

Sensitivity tests comparing the satellite-based fair-weather filter with a classical PG-range approach confirm that the pollutant-specific hierarchy and the dominant role of diurnal boundary-layer dynamics are robust to reasonable variations in filtering strategy. Similar pollutant-dependent behavior has recently been reported for the Tel Aviv metropolitan area, reinforcing the interpretation that PG–pollutant relationships in urban environments are governed primarily by emission timing, aerosol–ion interactions, and boundary-layer regime rather than by season alone (Yaniv et al., 2026).

5.2 Why São Paulo deviates from the Carnegie curve

The classical Carnegie curve represents the global mean diurnal variation of the PG under relatively clean and vertically well coupled conditions, and is commonly used as a reference for GAEC related modulation of fair weather PG measurements (Harrison, 2013; Harrison, 2020). However, near surface PG observations over land are known to be highly sensitive to local aerosol loading and atmospheric structure, particularly in polluted continental environments where local conductivity perturbations can dominate the surface signal (Harrison and Nicoll, 2018; Faruque et al., 2025).

In São Paulo, deviations from the Carnegie curve primarily reflect the dominance of persistent local electrical forcing rather than the absence of global scale GAEC modulation. Sustained urban emissions of aerosols and combustion related trace gases reduce near surface electrical conductivity and introduce strong horizontal and vertical gradients, producing PG variability that can rival or exceed the amplitude of the canonical Carnegie signal. Similar superposition of global and local electrical contributions has been documented within the South American AFINSA network, where systematic departures from the Carnegie

curve at São Paulo were attributed to urban pollution and boundary layer related conductivity effects (Tacza et al., 2020).

Boundary layer regime transitions further modulate this behavior. The Carnegie framework implicitly assumes efficient vertical electrical coupling between the surface and the free troposphere, an assumption that is frequently violated in large urban areas. In São Paulo, shallow and dynamically stable nocturnal boundary layers favor the accumulation of space charge near the surface, enhancing the influence of local conductivity perturbations on PG. During daytime, convective boundary layer development redistributes charge and conductivity vertically, partially restoring coupling to the overlying conduction current while introducing additional electrical variability associated with regional gradients and residual cloud structures (Li et al., 2023; Nicoll et al., 2022).

Overall, the observed distortions of the Carnegie curve at the surface, characterized by modified amplitude and symmetry while often preserving the diurnal phase, indicate that near surface PG in São Paulo reflects the superposition of a persistent global electric background with strong, regime dependent local conductivity control, rather than a breakdown of the GAEC framework itself.

5.3 Diurnal and regime control of PG–pollutant coupling

Across pollutants, the strongest and most consistent modulation of PG–pollutant relationships occurs at the diurnal timescale. Because the air-quality record is provided by a regulatory station located ~2 km from the PG sensor, the relationships reported here are interpreted at a central-urban (neighborhood-to-urban-core) scale rather than as a point-collocated proxy calibration. The key result is therefore the regime-dependent co-variability between electrically clean PG and the urban pollution state, not a street-scale mapping at the instrument location. Pronounced diurnal variability of PG measurements under fair-weather conditions has also been reported at polluted continental sites, where daytime weakening and nocturnal enhancement have been linked to aerosol loading and boundary-layer evolution (Li et al., 2025). The coupling strengthens during nocturnal hours, when the boundary layer is shallow and dynamically stable, as documented in observational studies of diurnal BLH variability (Gu et al., 2020), favoring pollutant accumulation near the surface and increasing the sensitivity of near-surface electrical conditions to changes in aerosol and trace-gas loading. Conversely, during the afternoon, convective turbulence deepens the boundary layer and enhances vertical mixing, which dilutes near-surface pollutant concentrations and reduces the coherence between PG and surface pollutant measurements, consistent with the role of boundary-layer depth in controlling effective dilution and surface representativeness (Kotthaus et al., 2023). This daytime “decoupling” is expected in megacity environments, where surface observations become less representative of the column-integrated pollutant burden and where additional electrical variability may arise from regional-scale conductivity contrasts and residual cloud influences, even under nominal fair-weather conditions.

An additional feature emerging from the wind-speed–resolved analysis is the presence of a distinct transition regime at moderate wind speeds. While most gaseous species exhibit a progressive weakening of PG correlations with increasing wind speed, in some cases approaching near-zero values without changing sign, PM_{10} displays a qualitatively different response. In winter, PG–PM_{10} correlations collapse rapidly near ~2.5–3.0 m s^{-1} and reverse sign at higher wind speeds. This behavior indicates a transition from accumulation-dominated conditions to a regime where mechanical resuspension, enhanced ventilation, and horizontal transport dominate the local PM_{10} burden. The absence of a comparable sign reversal for gaseous pollutants supports the interpretation that this transition is driven by particle-specific mechanical processes rather than by boundary-layer dilution alone.

The regime-dependent nature of this coupling explains the apparent contradiction between moderate seasonally averaged correlations (R = 0.5–0.6) and the near-unity correlations (R > 0.9) observed on specific stable days (as shown in Fig. 14). These high-correlation events serve as a proof-of-concept: they

demonstrate that the PG is intrinsically capable of tracking surface pollution with high fidelity. However, this capacity is strictly 'gated' by boundary-layer stability. When turbulent mixing dilutes the space-charge layer (daytime), the surface correlation collapses not because the electrical physics fails, but because the surface PG and surface pollutants are effectively measuring different atmospheric volumes. Thus, the lower average correlations reflect the frequency of convective decoupling, not a lack of sensor sensitivity.

Although boundary-layer height is not explicitly retrieved here, previous electrical profiling experiments have shown that strong convective mixing within the boundary layer is associated with a reduced vertical coherence of space-charge structures, whereas dynamically stable conditions favor a more vertically organized charge distribution and a surface electrical response that more directly reflects the underlying vertical charge structure (Nicoll et al., 2018). The regime-dependent behavior identified in São Paulo is therefore physically consistent with boundary-layer modulation of near-surface PG variability, rather than being primarily governed by pollutant-specific chemical effects.

The prominence of diurnal modulation provides an important interpretive constraint: seasonal differences in correlation strength are best understood as a secondary imprint mediated by seasonally varying stability, ventilation, and wind regimes, rather than as the primary organizing factor of PG–pollutant coupling once cloud-related electrical contamination is minimized.

5.4 Phase alignment and lag structure of PG–pollutant coupling

The lag patterns derived from cross correlation of the 168 hour weekly profiles reflect systematic phase relationships between PG and pollutant concentrations within the recurrent diurnal and weekly anthropogenic cycle, rather than fixed causal delays that would necessarily manifest in individual daily time series. In a megacity environment such as São Paulo, day to day variability in boundary layer development, synoptic ventilation, and local wind regimes can obscure reproducible short timescale lags when examined at event scale. However, when averaged across multi year fair weather conditions, consistent temporal alignments emerge that are robust to short term meteorological noise. A similar phase based interpretation of lag structure in averaged PG pollutant relationships has recently been applied in urban atmospheric electricity studies, where cross correlation was used to characterize recurrent diurnal and weekly coupling patterns rather than deterministic response times (Yaniv et al., 2026).

Primary combustion related gases, particularly NOx and CO, exhibit peak correlations at or near zero lag, indicating predominantly synchronous evolution with PG in the regime averaged cycle. This synchronicity is further confirmed by high Trend Match indices (>77%), demonstrating that the directional rate of change of the PG tracks primary emissions with high fidelity. This behavior is consistent with a rapid influence of fresh vehicular emissions on near surface electrical conditions through enhanced ion aerosol interactions that reduce electrical conductivity and increase PG under fair weather conditions. Nitric oxide shows a slight leading tendency, with peak correlation at a negative lag, consistent with its role as an early combustion tracer whose concentration can precede the maximum electrical response under stable nighttime conditions in the averaged cycle. Importantly, this leading behavior reflects a systematic phase relationship in the mean anthropogenic cycle rather than a fixed temporal precedence in individual daily series.

In contrast, NO2 and PM10 display delayed alignment relative to PG in the averaged profiles. This offset should not be interpreted as a deterministic response time, but rather as a repeatable phase shift within the composite diurnal and weekly cycle. For NO2, a positive lag is consistent with photochemical conversion of NO to NO2 within the evolving urban plume, which can shift concentration maxima relative to the timing of primary emissions and associated electrical response. For PM10, the delayed alignment is plausibly associated with a combination of slower microphysical influences on charge balance, such as ion particle attachment acting on evolving particle populations, and boundary layer or wind driven processes, including resuspension and transport, that can displace PM10 maxima relative to peak

emission activity. Notably, despite this delay, the PM10 Trend Match remains robust (~60%), significantly higher than values reported in other recent urban studies (e.g., Yaniv et al., 2026), suggesting that the PG-aerosol coupling in São Paulo preserves strong directional coherence even when phase-shifted.

Overall, the lag analysis indicates that PG pollutant coupling in São Paulo is governed by phase locked behavior tied to recurrent anthropogenic activity and boundary layer regimes, rather than by simple, fixed response times. These results reinforce the interpretation that near surface PG responds to pollution related electrical perturbations primarily within dynamically stable regimes, and that meaningful temporal structure emerges most clearly when local meteorological variability is averaged out over sufficiently long fair weather records.

5.5 Impacts of anthropogenic activity disruptions (truckers' strike, COVID-19 lockdowns)

Large-scale perturbations of anthropogenic emissions, such as the truckers' strike and the COVID-19 mobility restrictions, provide quasi-experimental opportunities to test whether the observed PG–pollutant coupling reflects genuine anthropogenic forcing rather than coincidental co-variability. Sustained reductions in traffic intensity are expected to decrease primary combustion markers such as NO, NO_x, and CO, thereby relaxing ion scavenging and partially restoring near-surface electrical conductivity. Under comparable fair-weather and boundary-layer conditions, such a relaxation should lead to a weakening of pollution-related PG enhancements. The observation of a coherent PG response during these periods, once cloud-related electrical disturbances and boundary-layer regime are controlled for, therefore strengthens the physical interpretation of the coupling.

At the same time, these natural experiments highlight important limitations. Changes in fleet composition, industrial activity, and regional transport differ across perturbation types, and meteorological conditions can vary substantially between pre-perturbation and perturbation periods. For this reason, the most defensible interpretation is necessarily comparative and regime-aware, focusing on fair-weather subsets and dynamically stable conditions rather than relying on simple differences in period-averaged means.

Interpreting the COVID-19 lockdown signal relative to the annual fair-weather baseline defined in Section 4.2 provides direct insight into anthropogenic modulation of the PG. Independent air-quality and mobility analyses demonstrate that the lockdown period in São Paulo was associated with a sustained reduction in traffic activity and primary pollutant concentrations, including CO, NO_2, and particulate matter, particularly during the most restrictive phase in April 2020 (Perez et al., 2022). This independent evidence provides a physically consistent external constraint for interpreting concurrent PG variability.

The annual fair-weather diurnal cycle shown in Figure 8a serves as a practical electrical reference for São Paulo under undisturbed conditions, reflecting the combined influence of global-scale GAEC forcing and persistent local boundary-layer processes. Relative to this baseline, the 2020 diurnal PG curve is systematically shifted toward lower values, frequently extending beyond the −1σ envelope, while preserving its overall diurnal structure. In particular, the characteristic morning enhancement and late-afternoon minimum remain clearly identifiable. This behavior indicates that the lockdown primarily affected the magnitude of the PG rather than its diurnal phase, implying that global-scale electrical forcing remained operative while local conductivity and space-charge conditions were modified.

A physically consistent interpretation involves a sustained reduction in anthropogenic aerosol and pollutant emissions during the lockdown, leading to increased near-surface electrical conductivity and reduced space-charge accumulation. Under such conditions, a broadly uniform decrease in fair-weather PG is expected, consistent with the observed downward displacement of the diurnal curve. The robustness of this interpretation is reinforced by the extensive fair-weather sampling during the lockdown period, particularly in April, which makes sampling artefacts an unlikely dominant explanation for the observed anomaly.

Comparable behavior has recently been reported for Buenos Aires, where fair-weather PG decreased systematically during the COVID-19 lockdown and was attributed to reduced vehicular activity and associated pollutant emissions (Velázquez et al., 2025). Taken together, the São Paulo and Buenos Aires results indicate that large-scale and sustained reductions in anthropogenic activity can produce measurable departures from the fair-weather electrical baseline in urban environments, even in the presence of strong and persistent diurnal modulation by the global atmospheric electric circuit.

5.6 Implications of PG-based machine learning results

Within the regime framework established in Sections 5.3–5.5, the machine-learning analysis provides an independent and complementary diagnostic perspective on the PG–pollutant coupling, rather than introducing a separate predictive objective. Its primary value lies in identifying the atmospheric conditions under which simple statistical representations remain physically meaningful, and those under which increased statistical flexibility merely accommodates regime mixing without restoring physical coherence.

Under stable nocturnal fair-weather conditions, the near-equivalence in performance between multiple linear regression and random forest models demonstrates that the dominant PG–pollutant covariation is well described by an approximately linear relationship. This behavior is consistent with a dynamically stable boundary-layer regime characterized by weak turbulence, limited vertical exchange, and gradual pollutant accumulation. In this regime, near-surface electrical conductivity responds in a quasi-linear manner to changes in aerosol and trace-gas loading, and increased model complexity does not yield additional explanatory power. The absence of any systematic advantage for non-linear models therefore reflects a physically gated regime, in which boundary-layer stability constrains the PG–pollutant relationship to a first-order response.

When the full diurnal cycle is considered, non-linear models exhibit modestly improved statistical skill relative to linear formulations. Importantly, this apparent gain does not indicate enhanced predictive power under physically degraded conditions. Instead, it reflects the aggregation of distinct dynamical regimes, stable nocturnal conditions and convectively mixed daytime states, within a single modeling framework. During daytime hours, rapid boundary-layer growth, enhanced turbulent mixing, and time-dependent changes in surface representativeness weaken the physical linkage between surface PG and surface pollutant concentrations. Under such conditions, similar pollutant concentrations may correspond to different electrical states depending on the prevailing dynamical context. Flexible models are therefore able to accommodate regime mixing more readily than a global linear fit, without resolving the underlying physical decoupling identified in Sections 5.3 and 5.4.

Crucially, the emergence of apparent non-linear skill during the full diurnal cycle does not imply that the PG responds to pollution in an intrinsically non-linear manner. Rather, it reflects increasing statistical complexity arising from meteorological modulation, boundary-layer evolution, and ventilation processes that progressively erode the vertical coherence of near-surface space-charge structures. The persistence of linear model adequacy under stable nocturnal conditions confirms that machine learning is not inherently required when the governing physical coupling is well constrained. Conversely, the degradation of predictive skill under convective daytime conditions demonstrates that increased model complexity cannot compensate for the breakdown of the physical assumptions linking near-surface PG to surface pollutant measurements.

Taken together, the machine-learning results reinforce the central conclusion of this study: the utility of PG as an indicator of urban pollution is fundamentally regime-dependent. Machine learning does not overcome this limitation but instead provides an independent confirmation of the same physical gating identified through correlation, wind-speed, and event-based analyses. Its role in this context is therefore diagnostic rather than predictive, highlighting when the atmospheric system behaves in an electrically ordered

manner and when dynamical mixing renders surface PG and surface pollution measurements intrinsically decoupled.

5.7 Implications for using PG as an air-pollution proxy

Taken together, the results of this study demonstrate that PG should not be interpreted as a quantitative proxy for urban air pollutant mass concentration, even under carefully filtered fair weather conditions. The moderate predictive skill obtained for PM10 and other pollutants, the strong asymmetry of correlation distributions, and the confinement of high PG pollutant coherence to specific temporal windows collectively indicate that PG does not provide a reliable surrogate measure of pollutant loading in a general sense. This conclusion is independently reinforced by the machine-learning results, which show that increased model complexity cannot recover predictive skill once the physical coupling between surface PG and surface pollutant concentrations is dynamically degraded.

Instead, the observations support a different and more physically consistent interpretation. PG acts as a sensitive indicator of regime transitions in which pollution related conductivity effects become dynamically relevant. Strong PG pollutant coupling preferentially emerges during nocturnally stable, weakly ventilated conditions, when near surface ion balance is most responsive to changes in aerosol and trace gas loading. Outside these regimes, particularly during daytime convective mixing, the electrical response becomes decoupled from surface pollutant concentrations despite the continued presence of emissions.

The stronger and more reproducible coupling observed for primary combustion related gases such as NOx and CO, compared to particulate matter, further supports this regime based interpretation. Gas phase pollutants directly modulate near surface ion attachment and conductivity, whereas PM10 is additionally influenced by wind driven resuspension and mechanical mixing, which can obscure any coherent electrical signature. Consequently, PG variability reflects the electrical sensitivity of the boundary layer, not pollutant concentration itself.

Within multi parameter urban observation networks, PG therefore adds value not as a replacement for chemical air quality measurements, but as an independent diagnostic of boundary layer regime and near surface conductivity state. When combined with basic dynamical context such as wind speed, stability proxies, and cloud screening, PG measurements provide insight into when and how anthropogenic pollution becomes electrically effective. This regime centered interpretation is consistent with earlier findings from the AFINSA network, which identified the Sao Paulo station as particularly sensitive to anthropogenic perturbations of PG, rather than as a universal proxy for pollutant mass concentration (Tacza et al., 2020).

6. Conclusions

This study examined the relationship between the PG and urban air pollution in the São Paulo metropolitan area using a long-term, multi-pollutant dataset under strictly defined fair-weather conditions. By combining surface meteorological screening with satellite-based cloud masking, the analysis isolates electrically undisturbed periods and provides a robust framework for interpreting PG variability in a complex megacity environment.

Across all analyses, boundary-layer regime emerges as the primary organizing control on PG–pollutant coupling. The strongest and most reproducible relationships occur during nocturnal, dynamically stable conditions, when pollutant accumulation near the surface enhances the sensitivity of near-surface electrical conductivity to anthropogenic emissions and produces a coherent PG response. In contrast, daytime convective mixing weakens this coupling and introduces additional electrical variability, leading to a systematic decoupling between PG and surface pollutant concentrations. Seasonal differences mainly modulate the amplitude of this behavior through their influence on atmospheric stability and ventilation, rather than acting as an independent organizing factor. Wind-speed–resolved analyses further reveal a

distinct transition regime, particularly for PM_{10}, in which mechanically driven processes dominate over accumulation and lead to a rapid collapse and inversion of PG correlations at moderate wind speeds.

Deviations from the classical Carnegie curve observed in São Paulo do not indicate a breakdown of the global atmospheric electric circuit, but instead reflect the superposition of strong local conductivity modulation and boundary-layer control on an underlying global signal. Urban aerosol and trace-gas emissions substantially modify PG under shallow nocturnal boundary layers, while daytime mixing and residual cloud influences distort the amplitude and symmetry of the canonical diurnal pattern without eliminating its overall phase structure.

Temporal alignment and trend matching analyses further show that PG–pollutant relationships are best interpreted in terms of phase-locked behavior within recurrent diurnal and weekly anthropogenic cycles, rather than as fixed causal response times. Primary combustion-related gases such as NOx and CO evolve largely synchronously with PG in the averaged cycle, exhibiting high directional coherence (>77% trend match). Whereas NO2 and PM10 exhibit systematic phase shifts consistent with photochemical processing and regime-dependent aerosol dynamics, they notably retain robust directional coupling, confirming that the electrical response to particulate matter persists despite the temporal lag. These patterns become most evident when local meteorological variability is averaged out over sufficiently long fair-weather records.

Large-scale emission perturbations associated with the COVID-19 lockdown provide independent support for the anthropogenic origin of the observed PG–pollutant coupling. The persistent reduction in fair-weather PG during 2020, accompanied by preservation of the diurnal phase structure, indicates that sustained decreases in urban emissions can measurably alter the magnitude of PG without disrupting global-scale electrical forcing. In contrast, shorter and weaker perturbations, such as the truckers' strike, do not produce a statistically distinct PG response, underscoring the importance of both the magnitude and duration of emission changes for producing a detectable electrical signal.

Machine-learning results are fully consistent with the physical interpretation derived from the observational analysis. Linear models perform comparably to non-linear approaches under stable nocturnal conditions, while predictive skill degrades markedly during daytime regimes characterized by enhanced turbulence. This behavior confirms that the usefulness of PG as an air-pollution indicator is fundamentally conditional and regime-dependent, and that increased model complexity cannot compensate for the breakdown of the underlying physical coupling.

Taken together, these findings demonstrate that PG should not be treated as a universal or quantitative proxy for urban air pollutant concentrations, even under carefully filtered fair-weather conditions. Instead, its primary value lies in diagnosing regime-dependent electrical sensitivity to anthropogenic emissions. When analyzed alongside basic dynamical context, including boundary-layer stability and wind conditions, PG measurements provide a complementary observational perspective on pollution-related conductivity changes and boundary-layer transitions that govern the temporal structure of urban air quality within multi-parameter monitoring networks.

Appendix A. Seasonal dependence of the wind speed–PG relationship

This fundamental relationship between wind speed and PG persists across all seasons, as illustrated in Figs. A1–A4. A coherent diurnal wind cycle is observed throughout the year, characterized by nocturnal to early-morning minima and a well-defined afternoon maximum. During winter, the timing of the wind speed maximum shifts slightly earlier (16:00–17:00 UTC), consistent with the seasonal modulation of the solar cycle and boundary-layer evolution.

A pronounced seasonal modulation is evident in the strength of the wind–PG coupling, while the inverse sign of the relationship is preserved in all seasons. The correlation is weakest during summer ($R \approx -0.15$

to −0.20; m ≈ −0.07 to −0.09 kV m⁻¹ per m s⁻¹) and progressively strengthens toward winter, when the largest magnitudes are observed (R ≈ −0.33 to −0.46; m ≈ −0.22 to −0.26 kV m⁻¹ per m s⁻¹). This seasonal enhancement is consistent with an increased effectiveness of wind-driven turbulent mixing in dispersing the near-surface space charge layer during the most atmospherically stable period of the year.

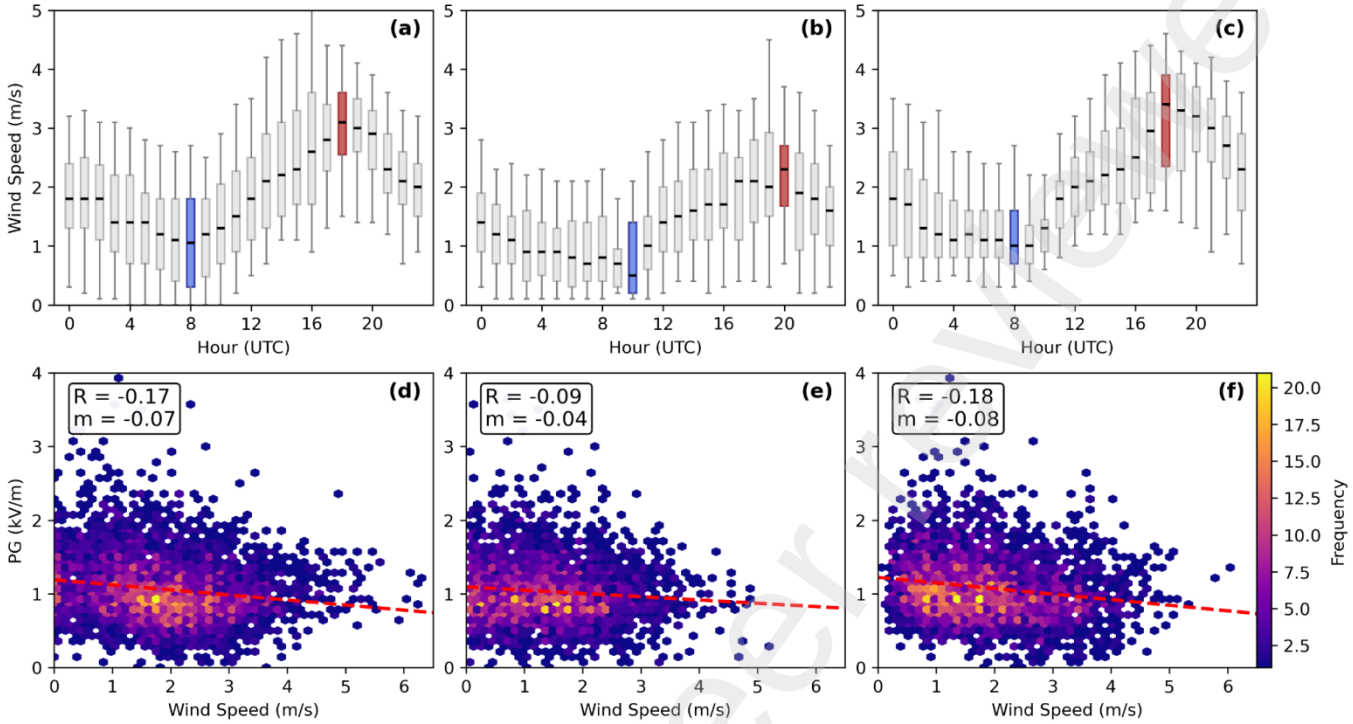

Figure A1. Seasonal dependence of wind speed and its relationship with PG during summer (DJF). Top: Hourly distribution of wind speed shown as boxplots for the Mirante, Interlagos, and Barueri stations. Bottom: Hexbin density plots showing the relationship between hourly wind speed and PG for each station.

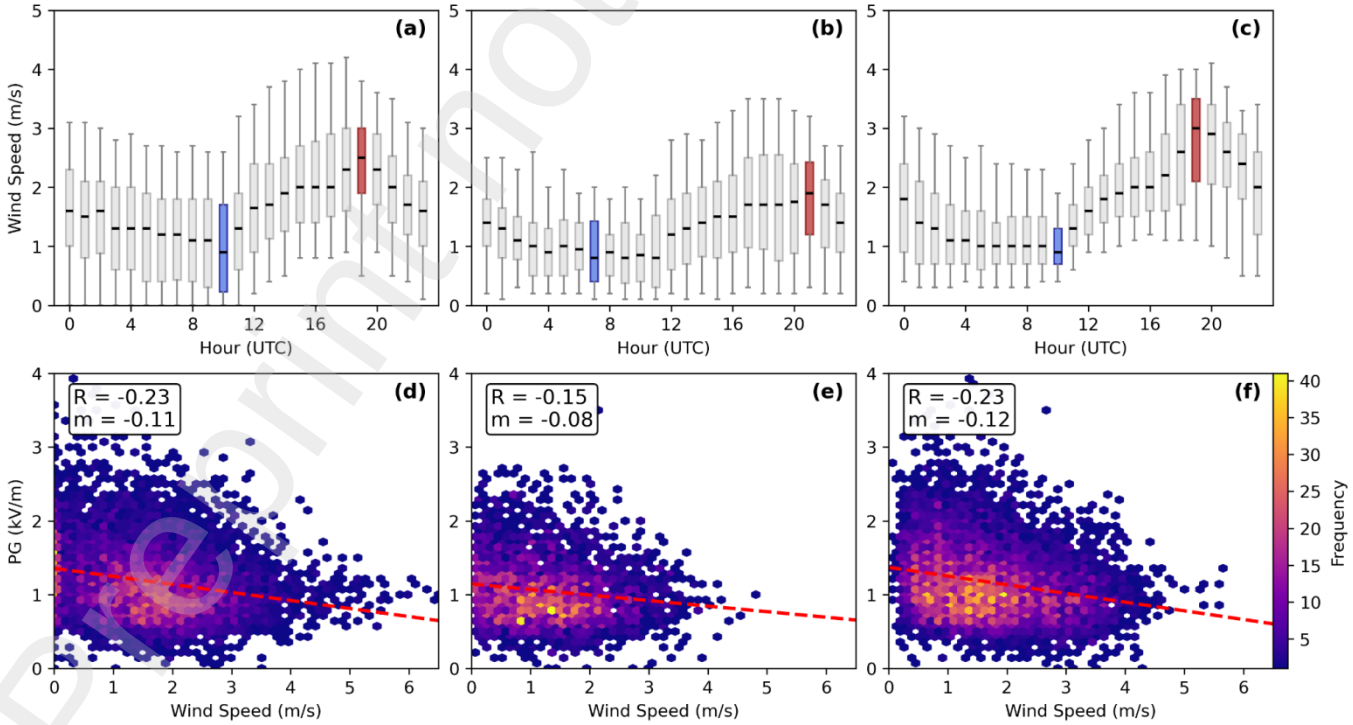

Figure A2. Same as Fig. A1, but for fall (MAM).

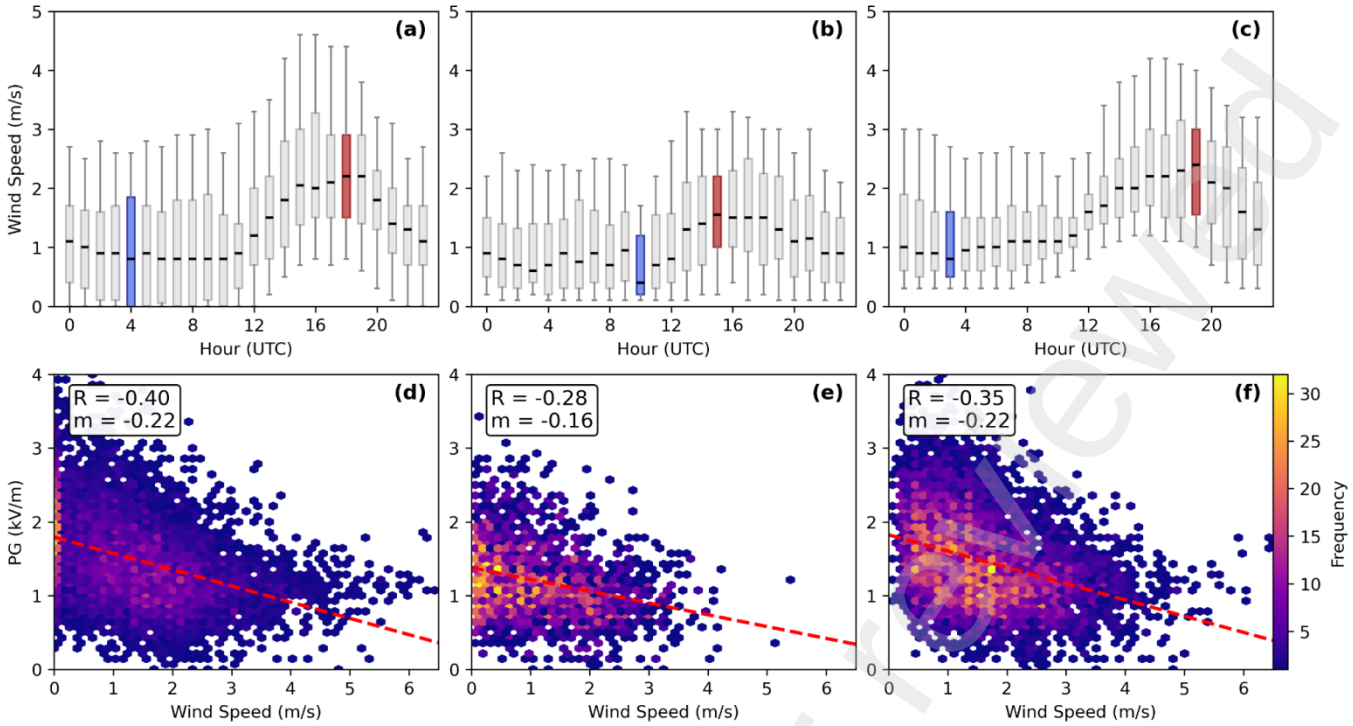

Figure A3. Same as Fig. A1, but for winter (JJA).

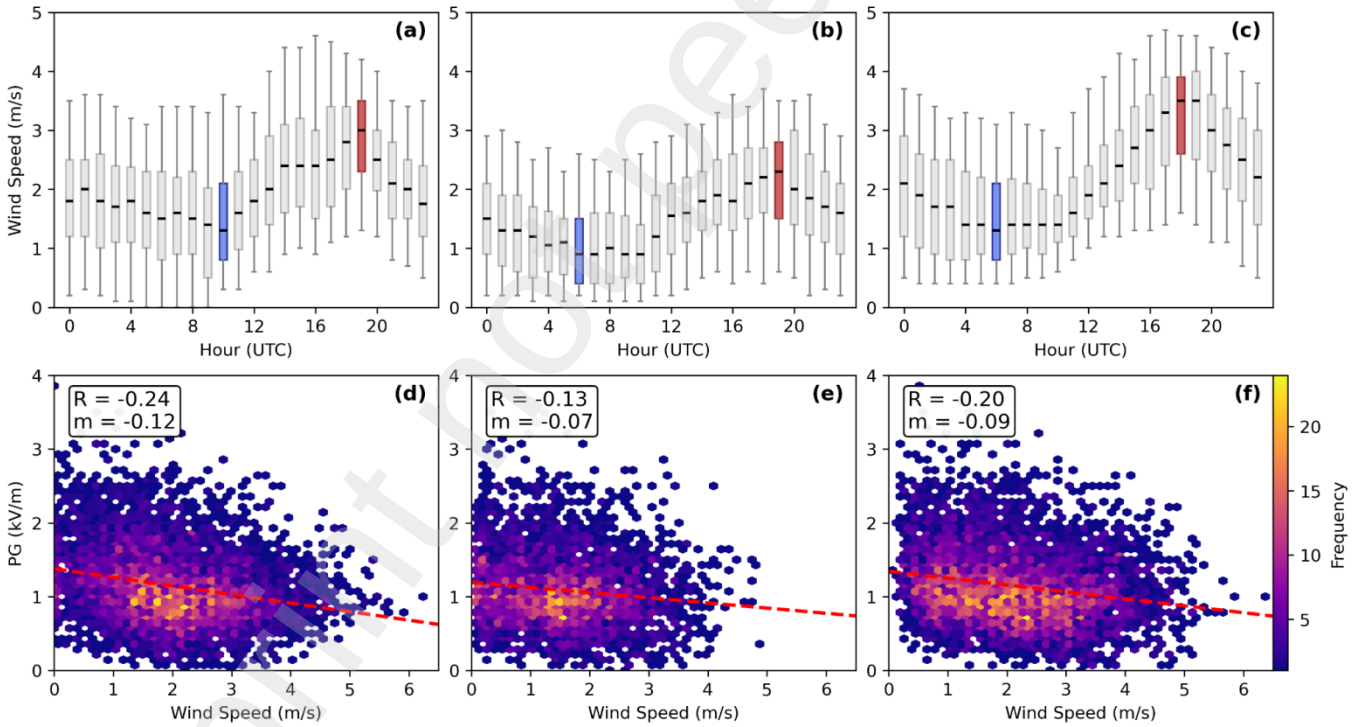

Figure A4. Same as Fig. A1, but for spring (SON).

Appendix B. Qualitative assessment of PG response during the COVID-19 lockdown at a low-emission site (Ica, Peru)

As a complementary case to the São Paulo analysis, PG observations from Ica, Peru, were examined during the early phase of the COVID-19 lockdown (Fig. B1). This site represents a contrasting environment, characterized by low anthropogenic emissions and dominant natural controls on near-surface atmospheric electricity.

The available PG record in Ica during the lockdown period is short, as measurements were interrupted on 22 March 2020 following the implementation of nationwide mobility restrictions. Consequently, the analysis is limited to the period 10–22 March and is interpreted qualitatively rather than statistically.

For consistency with earlier studies at this site, and due to the limited availability of continuous meteorological observations prior to 2020, fair-weather conditions were identified using an observational PG-range criterion (0–170 V m^{-1}), following the methodology proposed by Tacza et al. (2020) and previously applied by Romero et al. (2024). This approach differs from the meteorological and satellite-based filtering adopted for São Paulo and therefore does not allow a direct quantitative comparison between the two sites.

Within these constraints, the 2020 diurnal PG curve in Ica does not exhibit a clear or systematic reduction relative to adjacent pre-pandemic years. This behavior is consistent with the short duration of the available lockdown record and with the dominant role of natural drivers, such as boundary-layer dynamics, background aerosol loading, and regional meteorology, in controlling PG variability at this site.

The absence of a pronounced PG response in Ica contrasts with the persistent reduction observed in São Paulo during the COVID-19 lockdown and reinforces the interpretation that the São Paulo signal reflects a strong anthropogenic modulation of near-surface electrical conductivity rather than a global or universal pandemic-related effect. At low-emission sites such as Ica, reductions in human activity may be insufficient to produce an electrically detectable perturbation within the limits imposed by short observational windows.

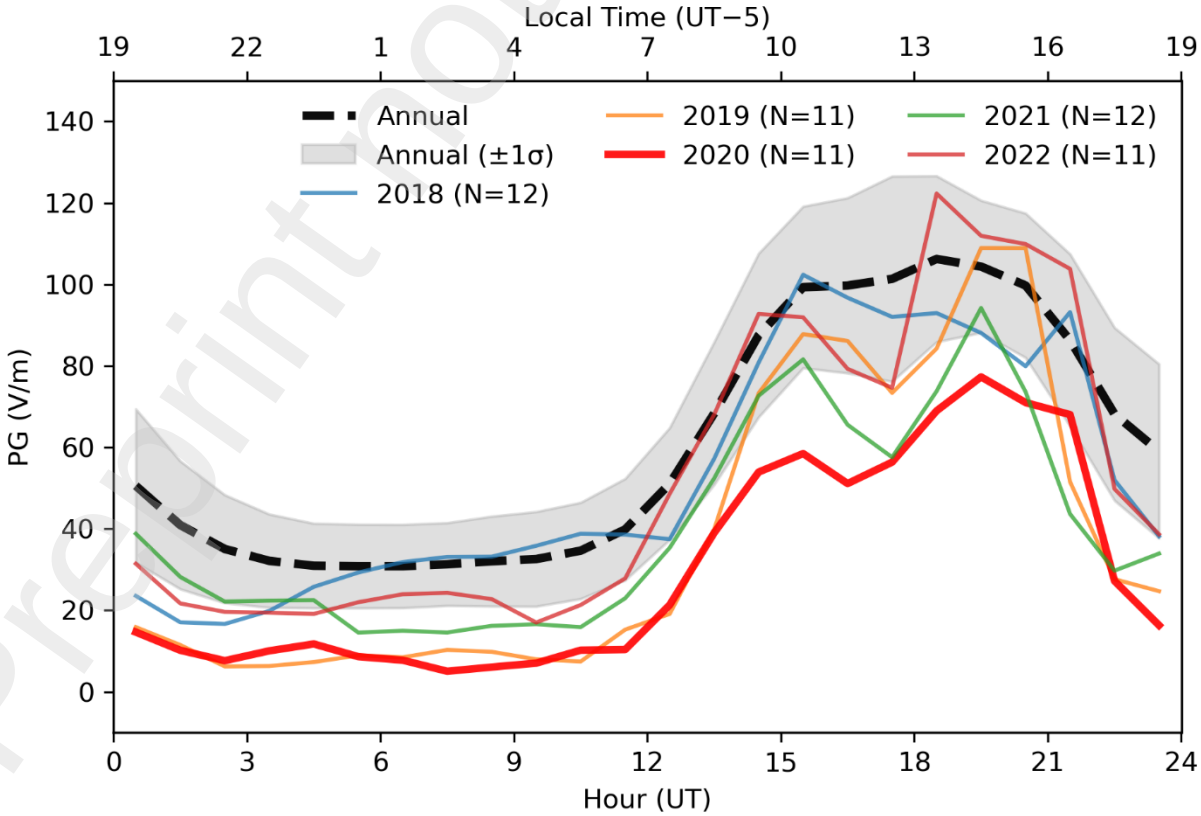

Figure B1. Fair-weather diurnal PG curves for Ica (Peru) computed over 10–22 March for individual years. Colored lines show year-specific diurnal means (mid-hour UTC), with the number of fair-weather day-equivalents (N) indicated in the legend. Fair-weather conditions were identified using a PG-range criterion (0–170 V m^{-1}) due to the limited availability of meteorological data prior to 2020. The dashed black line and gray shading represent the annual fair-weather baseline (mean ±1σ) derived from monthly diurnal curves across the 2018–2022 period.

CRediT author contributions

Rubén M. Romero: Conceptualization, Data curation, Methodology, Software, Formal analysis, Visualization, Writing – original draft.
J.C. Tacza: Conceptualization, Methodology, Writing – review & editing.
Angel Vara-Vela: Conceptualization, Writing – review & editing.
S. Szpigel: Supervision, Resources, Writing – review & editing.
J.-P. Raulin: Supervision, Resources, Writing – review & editing.

Acknowledgements

RR expresses gratitude to CNPq (Proc. 141576/2023-5 - GD). JPR thanks funding agencies CNPq (project:311927/2022-0) and CAPES (project:88881.310386/2018-697 01). J.T. acknowledges funding from the National Science Centre, Poland (Grant No. 2023/51/D/ST10/01757).

Declaration of competing interests

The authors declare that they have no competing interests.

Data availability statement

PG data belonging to The Atmospheric Electric Field Network in South America (AFINSA) used in this study are publicly available at https://doi.org/10.5281/zenodo.18582467. Air quality data were obtained from CETESB (https://arcgis.cetesb.sp.gov.br/), meteorological data from INMET (https://bdmep.inmet.gov.br/), and satellite composite imagery was accessed via the public CPTEC/INPE FTP repository (https://ftp.cptec.inpe.br).

Code availability

The code used in this study is not publicly available.

References

Andrade, M.D.F., Kumar, P., De Freitas, E.D., Ynoue, R.Y., Martins, J., Martins, L.D., Nogueira, T., Perez-Martinez, P., De Miranda, R.M., Albuquerque, T., Gonçalves, F.L.T., Oyama, B., Zhang, Y., 2017. Air quality in the megacity of São Paulo: Evolution over the last 30 years and future perspectives. Atmospheric Environment 159, 66–82. https://doi.org/10.1016/j.atmosenv.2017.03.051

Bao, R., Zhang, Y., Ma, B.J., Zhang, Z., He, Z., 2022. An Artificial Neural Network for Lightning Prediction Based on Atmospheric Electric Field Observations. Remote Sensing 14, 4131. https://doi.org/10.3390/rs14174131

Bennett, A.J., Harrison, R.G., 2007. Atmospheric electricity in different weather conditions. Weather 62, 277–283. https://doi.org/10.1002/wea.97

Bernacki, J., Scherer, R., 2025. A comprehensive review of data-driven techniques for air pollution concentration forecasting. Sensors 25, 6044. https://doi.org/10.3390/s25196044

CETESB, 2005. Caracterização das estações da rede automática de monitoramento da qualidade do ar na RMSP: estação Cerqueira César. Companhia Ambiental do Estado de São Paulo, São Paulo, Brazil. https://repositorio.cetesb.sp.gov.br/handle/123456789/1993

Chalmers, J.A., 1954. Atmospheric electricity. Reports on Progress in Physics 17(1), 101–133. https://doi.org/10.1088/0034-4885/17/1/303

Cobb, W.E., 1973. Oceanic Aerosol Levels Deduced from Measurements of the Electrical Conductivity of the Atmosphere. J. Atmos. Sci. 30, 101–106. https://doi.org/10.1175/1520-0469(1973)

Coelho, S., Ferreira, J., Lopes, M., 2023. Source apportionment of air pollution in urban areas: a review of the most suitable source-oriented models. Air Qual Atmos Health 16, 1185–1194. https://doi.org/10.1007/s11869-023-01334-z

Dhanorkar, S., Kamra, A.K., 1992. Relation between electrical conductivity and small ions in the presence of intermediate and large ions in the lower atmosphere. J. Geophys. Res. 97, 20345–20360. https://doi.org/10.1029/92JD01915

Faruque, R.A., Pal, S., Amin, G., Mondal, S.K., 2025. Atmospheric electric field variations and its correlation with air quality index as observed from two low-latitude Indian stations. Journal of Atmospheric and Solar-Terrestrial Physics 271, 106505. https://doi.org/10.1016/j.jastp.2025.106505

Gu, J., Zhang, Y., Yang, N., Wang, R., School of Hydrology and Water Resources, Nanjing University of Information Science and Technology, Nanjing 210044, China, State Oceanic Administration Key Laboratory for Polar Science, Polar Research Institute of China, Shanghai 200136, China, 2020. Diurnal variability of the planetary boundary layer height estimated from radiosonde data. Earth and Planetary Physics 4, 1–14. https://doi.org/10.26464/epp2020042

Guo, T., Liu, R., Yang, H., Shi, L., Li, F., Zhang, L., Chen, Y., Liu, Z., Luo, F., 2017. Predict Atmosphere Electric Field Value with the LSTM Neural Network, in: 2017 International Conference on Computer Systems, Electronics and Control (ICCSEC). Presented at the 2017 International Conference on Computer Systems, Electronics and Control (ICCSEC), IEEE, Dalian, pp. 263–266. https://doi.org/10.1109/ICCSEC.2017.8447009

Harrison, R.G., Aplin, K.L., 2002. Mid-nineteenth century smoke concentrations near London. Atmospheric Environment 36, 4037–4043. https://doi.org/10.1016/S1352-2310(02)00334-5

Harrison, R., Aplin, K.L., 2003. Nineteenth century Parisian smoke variations inferred from Eiffel Tower atmospheric electrical observations. Atmospheric Environment 37, 5319–5324. https://doi.org/10.1016/j.atmosenv.2003.09.042

Harrison, R.G., Carslaw, K.S., 2003. Ion-aerosol-cloud processes in the lower atmosphere. Reviews of Geophysics 41, 2002RG000114. https://doi.org/10.1029/2002RG000114

Harrison, R.M., Jones, A.M., 2005. Multisite Study of Particle Number Concentrations in Urban Air. Environ. Sci. Technol. 39, 6063–6070. https://doi.org/10.1021/es040541e

Harrison, R.G., 2013. The Carnegie Curve. Surv Geophys 34, 209–232. https://doi.org/10.1007/s10712-012-9210-2

Harrison, R.G., Nicoll, K.A., 2018. Fair weather criteria for atmospheric electricity measurements. Journal of Atmospheric and Solar-Terrestrial Physics 179, 239–250. https://doi.org/10.1016/j.jastp.2018.07.008

Karagioras, A., Kourtidis, K., 2021. A Study of the Effects of Rain, Snow and Hail on the Atmospheric Electric Field near Ground. Atmosphere 12, 996. https://doi.org/10.3390/atmos12080996

Karmoude, M., Munhungewarwa, B., Chiraira, I., Mckenzie, R., Kong, J., Smith, B., Ayana, G., Njara, N., Mathaha, T., Kumar, M., Mellado, B., 2025. Machine learning for air quality prediction and data analysis: Review on recent advancements, challenges, and outlooks. Science of The Total Environment 1002, 180593. https://doi.org/10.1016/j.scitotenv.2025.180593

Khaled, A., Elsir, A.M.T., Shen, Y., 2022. GSTA: gated spatial–temporal attention approach for travel time prediction. Neural Comput & Applic 34, 2307–2322. https://doi.org/10.1007/s00521-021-06560-z

Kotthaus, S., Bravo-Aranda, J.A., Collaud Coen, M., Guerrero-Rascado, J.L., Costa, M.J., Cimini, D., O'Connor, E.J., Hervo, M., Alados-Arboledas, L., Jiménez-Portaz, M., Mona, L., Ruffieux, D., Illingworth, A., Haeffelin, M., 2023. Atmospheric boundary layer height from ground-based remote sensing: a review of capabilities and limitations. Atmos. Meas. Tech. 16, 433–479. https://doi.org/10.5194/amt-16-433-2023

Leirião, L.F.L., Debone, D., Pauliquevis, T., Rosário, N.M.É.D., Miraglia, S.G.E.K., 2020. Environmental and public health effects of vehicle emissions in a large metropolis: Case study of a truck driver strike in Sao Paulo, Brazil. Atmospheric Pollution Research 11, 24–31. https://doi.org/10.1016/j.apr.2020.02.020

Li, Y., Li, J., Zhao, Yuxin, Lei, M., Zhao, Yang, Jian, B., Zhang, M., Huang, J., 2021. Long-term variation of boundary layer height and possible contribution factors: A global analysis. Science of The Total Environment 796, 148950. https://doi.org/10.1016/j.scitotenv.2021.148950

Li, L., Chen, T., Song, J., Ti, S., Wang, S., Cai, C., Li, W., Luo, J., 2023. Comparison of the Atmospheric Electric Field from Three Global Stations in 2021. Universe 9, 112. https://doi.org/10.3390/universe9030112

Li, R., Ti, S., Li, L., Song, J., Chen, T., 2025. Diurnal variations of atmospheric electric fields on fair weather days and its correlations with aerosols, wind speed, irradiance, and relative humidity. Sci Rep 15, 7030. https://doi.org/10.1038/s41598-025-89788-2

Mauchly, S.J., 1923. On the diurnal variation of the potential gradient of atmospheric electricity. Terr Magneti and Atmo Electr 28, 61–81. https://doi.org/10.1029/TE028i003p00061

Mohammed, A.M., Saleh, I.A., M Abdel-Latif, N., 2020. Review article: air quality and characteristics of sources. IJBSBE 6, 85–91. https://doi.org/10.15406/ijbsbe.2020.06.00193

Moreira, G.D.A., Marques, M.T.A., Lopes, F.J.D.S., Andrade, M.D.F., Landulfo, E., 2024. Analyzing the influence of the planetary boundary layer height, ventilation coefficient, thermal inversions, and aerosol optical Depth on the concentration of PM2.5 in the city of São Paulo: A long-term study. Atmospheric Pollution Research 15, 102179. https://doi.org/10.1016/j.apr.2024.102179

Nicoll, K.A., Harrison, R.G., Silva, H.G., Salgado, R., Melgâo, M., Bortoli, D., 2018. Electrical sensing of the dynamical structure of the planetary boundary layer. Atmospheric Research 202, 81–95. https://doi.org/10.1016/j.atmosres.2017.11.009

Nicoll, K.A., Readle, A., Al Kamali, A., Harrison, R.G., 2022. Surface atmospheric electric field variability at a desert site. Journal of Atmospheric and Solar-Terrestrial Physics 241, 105977. https://doi.org/10.1016/j.jastp.2022.105977

Pawlak, I., Odzimek, A., Kępski, D., Tacza, J., 2025. Diurnal, seasonal, and annual variations of the fair-weather atmospheric potential gradient and effects of reduced number concentration of condensation

nuclei on potential gradient and air conductivity from long-term atmospheric electricity measurements at Świder, Poland. Ann. Geophys. 43, 391–416. https://doi.org/10.5194/angeo-43-391-2025

Pereira, G.M., Da Silva Caumo, S.E., Grandis, A., Do Nascimento, E.Q.M., Correia, A.L., De Melo Jorge Barbosa, H., Marcondes, M.A., Buckeridge, M.S., De Castro Vasconcellos, P., 2021. Physical and chemical characterization of the 2019 “black rain” event in the Metropolitan Area of São Paulo, Brazil. Atmospheric Environment 248, 118229. https://doi.org/10.1016/j.atmosenv.2021.118229

Peng, Z., Zhang, B., Wang, D., Niu, X., Sun, J., Xu, H., Cao, J., Shen, Z., 2024. Application of machine learning in atmospheric pollution research: A state-of-art review. Science of The Total Environment 910, 168588. https://doi.org/10.1016/j.scitotenv.2023.168588

Pérez-Martínez, P.J., Magalhães, T., Maciel, I., De Miranda, R.M., Kumar, P., 2021. Effects of the COVID-19 Pandemic on the Air Quality of the Metropolitan Region of São Paulo: Analysis Based on Satellite Data, Monitoring Stations and Records of Annual Average Daily Traffic Volumes on the Main Access Roads to the City. Atmosphere 13, 52. https://doi.org/10.3390/atmos13010052

Piper, I.M., Bennett, A.J., 2012. Observations of the atmospheric electric field during two case studies of boundary layer processes. Environ. Res. Lett. 7, 014017. https://doi.org/10.1088/1748-9326/7/1/014017

Ribeiro, F.N.D., Oliveira, A.P.D., Soares, J., Miranda, R.M.D., Barlage, M., Chen, F., 2018. Effect of sea breeze propagation on the urban boundary layer of the metropolitan region of Sao Paulo, Brazil. Atmospheric Research 214, 174–188. https://doi.org/10.1016/j.atmosres.2018.07.015

Romero, R., Tacza, J., Arroyo, J., Prieto, F., Macotela, L., Buleje, Y., Loayza, R., Fernandez, U., Raulin, J.-P., 2024. First results of the potential gradient variation in a tropical station in South America (Ica, Peru). Journal of Atmospheric and Solar-Terrestrial Physics 256, 106198. https://doi.org/10.1016/j.jastp.2024.106198

Romero Ramirez, R.M. (2026) «Hourly Atmospheric Potential Gradient Data from São Paulo (SPA) station - CRAAM (2018–2024)». Zenodo. doi:10.5281/zenodo.18582467.

Rycroft, M.J., Israelsson, S., Price, C., 2000. The global atmospheric electric circuit, solar activity and climate change. Journal of Atmospheric and Solar-Terrestrial Physics 62, 1563–1576. https://doi.org/10.1016/S1364-6826(00)00112-7

Rycroft, M.J., 2025. Some Recent Key Aspects of the DC Global Electric Circuit. Atmosphere 16, 348. https://doi.org/10.3390/atmos16030348

Sheftel, 1994. Air conductivity and atmospheric electric field as an indicator of anthropogenic atmospheric pollution. J. Geophys. Res. 99, 10793–10795. https://doi.org/10.1029/94JD00287

Silva, H.G., Conceição, R., Melgão, M., Nicoll, K., Mendes, P.B., Tlemçani, M., Reis, A.H., Harrison, R.G., 2014. Atmospheric electric field measurements in urban environment and the pollutant aerosol weekly dependence. Environ. Res. Lett. 9, 114025. https://doi.org/10.1088/1748-9326/9/11/114025

Silva, H.G., Conceição, R., Khan, M.A.H., Matthews, J.C., Wright, M.D., Collares-Pereira, M., Shallcross, D.E., 2016. Atmospheric electricity as a proxy for air quality: Relationship between potential gradient and pollutant gases in an urban environment. Journal of Electrostatics 84, 32–41. https://doi.org/10.1016/j.elstat.2016.08.006

Soria, J.J., Sumire, D.A., Poma, O., Saavedra, C.E., 2020. Neural Network Model with Time Series for the Prediction of the Electric Field in the East Lima Zone, Peru, in: Silhavy, R. (Ed.), Artificial Intelligence and

Bioinspired Computational Methods, Advances in Intelligent Systems and Computing. Springer International Publishing, Cham, pp. 395–410. https://doi.org/10.1007/978-3-030-51971-1_33

Tacza, J., Raulin, J.-P., Macotela, E., Marun, A., Fernandez, G., Bertoni, F.C.P., Lima, L.M., Samanes, J., Buleje, Y., Correia, E., Alves, G., Makita, K., 2020. Local and global effects on the diurnal variation of the atmospheric electric field in South America by comparison with the Carnegie curve. Atmospheric Research 240, 104938. https://doi.org/10.1016/j.atmosres.2020.104938

Uba, D.M., Machado, L.A.T., Pereira, S.P., de Souza, D.R.M., Negri, R.G. and Batista, R.S., 2023. *DSAT: Aplicação para visualização interativa dos dados recebidos pela estação GOES-R do INPE*. Anais do XX Simpósio Brasileiro de Sensoriamento Remoto (SBSR). São José dos Campos: Instituto Nacional de Pesquisas Espaciais (INPE). Available at: https://proceedings.science/sbsr-2023/dsat

Vara-Vela, A., De Fátima Andrade, M., Zhang, Y., Kumar, P., Ynoue, R.Y., Souto-Oliveira, C.E., Da Silva Lopes, F.J., Landulfo, E., 2018. Modeling of Atmospheric Aerosol Properties in the São Paulo Metropolitan Area: Impact of Biomass Burning. JGR Atmospheres 123, 9935–9956. https://doi.org/10.1029/2018JD028768

Vara-Vela, A.L., Herdies, D.L., Alvim, D.S., Vendrasco, É.P., Figueroa, S.N., Pendharkar, J., Reyes Fernandez, J.P., 2021. A New Predictive Framework for Amazon Forest Fire Smoke Dispersion over South America. Bulletin of the American Meteorological Society 102, E1700–E1713. https://doi.org/10.1175/BAMS-D-21-0018.1

Velazquez, Y.R., Nicora, M.G., Galligani, V.S., Wolfram, E.A., D'Elia, R.L., 2025. Fair weather electric field variability in Buenos Aires: The role of traffic and pandemic lockdowns. Atmospheric Research 321, 108087. https://doi.org/10.1016/j.atmosres.2025.108087

Whipple, F.J.W., 1929. Potential gradient and atmospheric pollution : The influence of "summer time." Quart J Royal Meteoro Soc 55, 351–362. https://doi.org/10.1002/qj.49705523206

Wilson, C.T.R., 1921. III. Investigations on lighting discharges and on the electric field of thunderstorms. Philosophical Transactions of the Royal Society of London. Series A, Containing Papers of a Mathematical or Physical Character 221, 73–115. https://doi.org/10.1098/rsta.1921.0003

Wright, M.D., Matthews, J.C., Silva, H.G., Bacak, A., Percival, C., Shallcross, D.E., 2020. The relationship between aerosol concentration and atmospheric potential gradient in urban environments. Science of The Total Environment 716, 134959. https://doi.org/10.1016/j.scitotenv.2019.134959

Yaniv, R., Froomer, I., Yair, Y., Hochman, A., 2026. Effects of urban air pollution on the fair-weather electric field in the Tel-Aviv, Israel metropolitan area. Atmospheric Research 331, 108661. https://doi.org/10.1016/j.atmosres.2025.108661

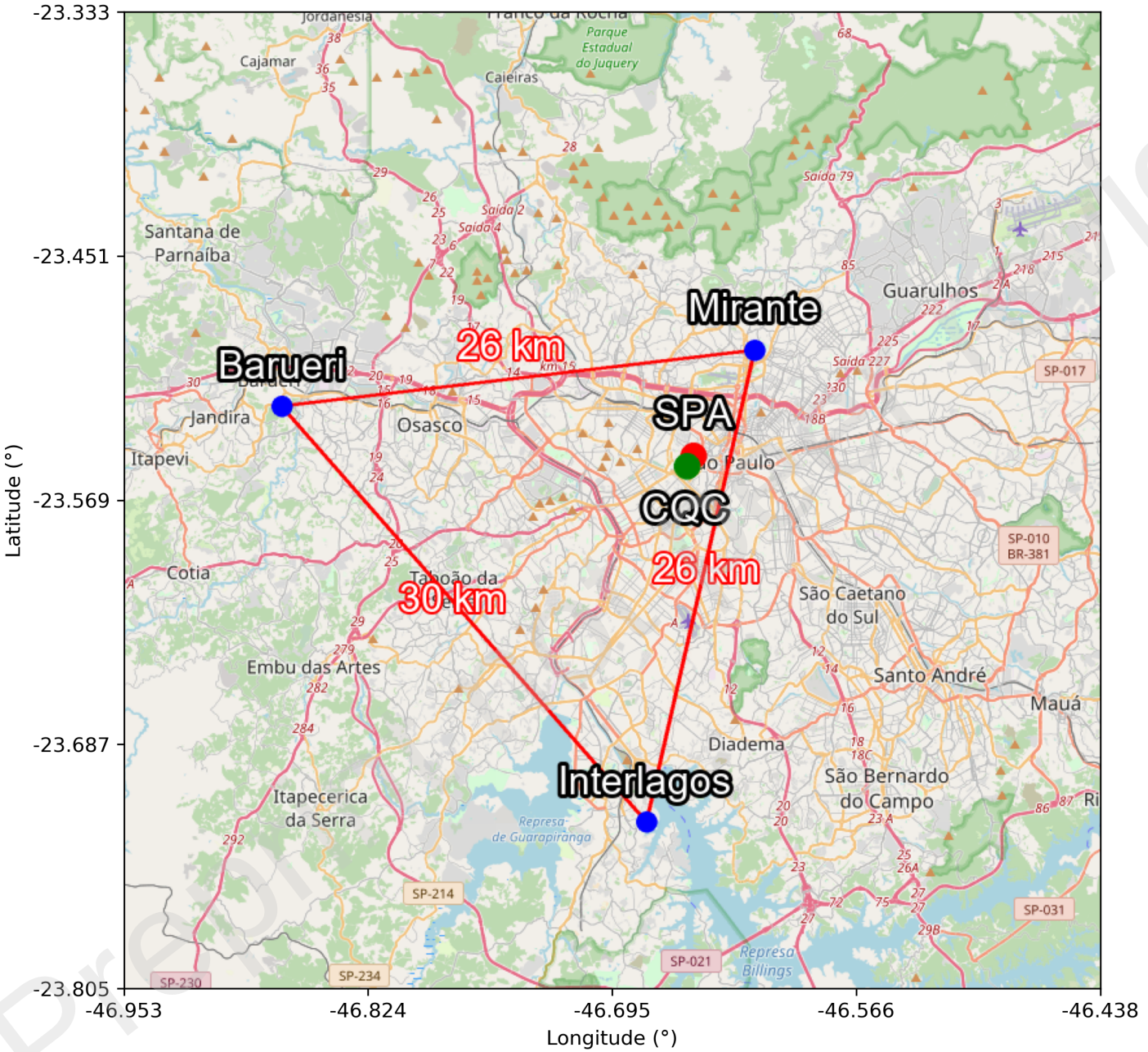
-23.333
-23.451
-23.569
-23.687
-23.805
Latitude (°)
-46.953
-46.824
-46.695
-46.566
-46.438
Longitude (°)
Barueri
Mirante
SPA
CQC
Interlagos
26 km
26 km
30 km
Jordanésia
Cajamar
Caieiras
Parque Estadual do Juquery
Santana de Parnaíba
Guarulhos
Jandira
Osasco
Itapevi
Cotia
Taboão da Serra
São Caetano do Sul
Santo André
Mauá
Diadema
São Bernardo do Campo
Embu das Artes
Itapecerica da Serra
Represa de Guarapiranga
Represa Billings
SP-017
SP-010
BR-381
SP-214
SP-234
SP-230
SP-021
SP-031